

## Article

# Advanced Mud Displacement Modeling for Slim Hole Cementing Operations

Ningyu Wang <sup>1,\*</sup>, Christopher Lamb <sup>1</sup>, Pradeepkumar Ashok <sup>1</sup>, Eric van Oort <sup>1,\*</sup>, Garrett Granier <sup>2</sup> and Tatiana Gobert <sup>2</sup>

<sup>1</sup> Hildebrand Department of Petroleum and Geosystems Engineering, The University of Texas at Austin, Austin, TX 78712, USA

<sup>2</sup> Occidental, Houston, TX 77046, USA

\* Correspondence: wny001@sina.com (N.W.); vanoort@austin.utexas.edu (E.v.O.)

**Abstract:** Successful design and execution of slim-hole cementing operations depend on reliable prediction of the annular pressure and the efficiency of mud displacement by cement. A 3D model of the flow inside the casing and in the annulus during mud displacement/cement placement operations was created. The yield-power-law fluid model was used for the rheological behavior of mud, spacers, and cement. Mud displacement was analyzed by splitting the well into multiple sections and analyzing the efficiency of mud removal by spacers and cement, as well as the associated pressure gradients in each section for applicable combinations of pump rate and casing rotation speed. The results from the various computational steps were then integrated to compute the overall pressure and cement placement efficiency during the cementing operation. Using the new 3D model, a field case study was performed for a slim hole casing cementation on an unconventional shale well. The simulated peak surface pressure was only 0.3% lower than the measured data, and the trend of the pressure matched the measured data. This work provides a new tool for the well construction industry to predict and analyze the pressure during complicated cementing operations, thereby enabling safer and more cost-effective operations.

**Keywords:** mud displacement; 3D modeling; pressure analysis; surface pressure; pump rate



**Citation:** Wang, N.; Lamb, C.; Ashok, P.; van Oort, E.; Granier, G.; Gobert, T. Advanced Mud Displacement Modeling for Slim Hole Cementing Operations. *Energies* **2024**, *17*, 1226. <https://doi.org/10.3390/en17051226>

Academic Editors: Mofazzal Hossain and S.M. Farouq Ali

Received: 13 December 2023

Revised: 16 February 2024

Accepted: 26 February 2024

Published: 4 March 2024



**Copyright:** © 2024 by the authors. Licensee MDPI, Basel, Switzerland. This article is an open access article distributed under the terms and conditions of the Creative Commons Attribution (CC BY) license (<https://creativecommons.org/licenses/by/4.0/>).

## 1. Introduction

Cementing is a pivotal step in well construction [1–4]. Cement acts as a barrier that seals the gap between casing strings and wellbore sections, thereby isolating zones of varying subsurface pressure and mechanically securing and supporting the casing. Improper cement placement may compromise well integrity, in turn potentially leading to safety incidents and environmental upsets (such as fluid leaks to the surface, gas emissions to air, etc.).

During cement placement, the annular drilling fluid (mud) is replaced by cement. The quality of the cement displacement can be quantified by the cement displacement efficiency (CDE) and is defined by the volume fraction of cement in a cross-section in the annulus [2]. If non-displaced drilling fluid is left in the annulus, it may contaminate the cement and prevent it from setting and sealing properly, leading to safety, economic, and environmental issues (associated with a lack of zonal isolation and poor well integrity). The non-displaced drilling fluid also decreases the equivalent flow path cross-section area for the cement and thus increases the pressure gradient.

In slim hole cementing operations, improper pressure estimation has become a major concern, even in the absence of CDE problems. Underestimating pressure can lead to significant delays and increased expenses, as peak surface pressure is an important design parameter for determining the required surface pumping equipment. If the peak surface pressure is underestimated during the design phase, the equipment used may lack the

capability to perform the cement job as planned. Failure to properly estimate peak pressure has caused significant operation delays and economic losses in the field. At the same time, maintaining pressure within set limits, similar to drilling operations, is essential to prevent wellbore damage. Excessive pressure in the annulus, particularly at the bottom hole location, can fracture the formation. This can, in turn, result in circulation loss and formation damage.

Cement displacement is impacted by a variety of factors, such as the properties of the drilling fluid, the flow regime, the flow rate, the annulus geometry [1,3], etc. Early numerical studies, such as those reported by McLean et al. [5] and Beirute and Flumerfelt [6], focused on modeling the flow pattern in a cross-section in the annulus. Even today, interface stability is still actively investigated to improve the CDE [7,8].

In more recent years, 3D models have been established to investigate more complicated cases, as shown in Table 1. Savery et al. [9] proposed a 3D finite difference model of two-phase flow in the annulus as a tool for studying the cement front. They ignored the axial and azimuthal velocities as well as the azimuthal pressure gradient in the tangential momentum equation. This model was later adopted to study the intermixing at the cement front [10] and the free fall of the cement in the casing while the flow in the annulus is single-phase [11]. Chen et al. [12] reported a 3D finite difference model without details of the model to study the intermixing. Enayatpour and van Oort [2] developed a 3D finite volume model based on the volume of fluid (VOF) method to study the frictional pressure and CDE and found that pipe rotation and higher eccentricity decrease the frictional pressure while pipe rotation and lower eccentricity improve the CDE, with pipe rotation being able to partially offset the negative effects of higher eccentricity on CDE. Gao et al. [13] applied this model and found that the wellbore size has a significant impact on the pressure gradient. Bu et al. [14] subsequently deployed this model on a different software platform and found that a higher density difference between the mud and the cement first increases and then decreases the CDE. Tardy and Bittleston [15] created a (2+1)D finite volume method with a narrow gap assumption and averaging the fluid volume fraction and velocity along the radial direction to study the mud displacement in the annulus. Based on this model, Tardy et al. [16] presented a simplified 3D model of the entire wellbore by segmenting the wellbore into many sections and analyzing the cement displacement in each section. This model was later used to analyze a few wells in the Gulf of Mexico [17]. To improve the accuracy of this model, Tardy [18] kept the narrow gap assumption but introduced a radial variation of the averaged parameters and proposed that the model may still be less computationally expensive than a full-scale 3D model. However, Tardy's model underestimates the pressure gradient, especially at high eccentricity ( $>0.3$ ). By further assuming the flow pattern at the widest and narrowest parts of the annulus, Foroushan et al. [19] created a semi-analytical 3D model with a sequential solution of the single-phase flow plus a partial differential equation for the two-phase interface. Maleki and Frigaard [20] also built a 3D model based on the narrow gap assumption and used it to study primary cementing [21]. Zhang et al. [22] developed a 3D model to study the flow around the centralizer during cementing to compare the nonspiral and spiral flow displacement.

In addition to the above 'traditional' models based on Navier–Stokes equations, Li and Novotny [23] and Grasinger et al. [24] each proposed a 2D Lattice–Boltzmann model for pipe flow and suggested possible application in the annulus.

This paper introduces a 3D finite volume model for the entire cement displacement process. It builds upon the submodel developed by Enayatpour and van Oort [2], which modeled flow in a well section without assuming a narrow gap. We have integrated this submodel to analyze the full cement displacement operation in a well. Our model's capability to simulate CDE assists high-precision pressure analysis during cement placement and mud/spacer displacement because the CDE impacts the pressure gradient by impacting the cross-sectional area of the cement flow. We demonstrate the model's enhanced precision through a field case study. Here, we compare our pressure prediction results with those from a commercial model, whose output had significant discrepancies with actual

cementing field data. Additionally, the developed model allows us to explore the impact of wellbore diameter distribution on pressure estimation.

**Table 1.** Recent numerical models for cement displacement analysis.

Paper	Model	Simplification of Conservation Equations	Application
[9–11]	3D finite difference.	Ignored the axial and azimuthal velocities as well as the azimuthal pressure gradient in the tangential momentum equation.	Velocity profile of the annular two-phase flow. Free fall of cement in the pipe.
[12]	Not reported.	Not reported.	Intermixing of mud and cement.
[2,13,14]	3D finite volume.	None.	Pressure gradient and cement displacement efficiency in a section in the annulus.
[15–17,20,21]	(2+1)D finite volume.	Narrow gap assumption. Averaged the fluid volume fraction and velocity along the radial direction.	Pressure gradient and cement displacement efficiency in a section in the annulus. Pressure in the annulus during cement placement.
[18]	3D finite volume.	Narrow gap assumption with radial variation of averaged fluid volume fraction and velocity.	Pressure gradient and cement displacement efficiency in a section in the annulus.
[19]	3D semi-analytical. Sequential solution.	Narrow gap assumption. Assumed flow pattern at the widest and narrowest parts of the annulus.	Pressure gradient and cement displacement efficiency in a section in the annulus.
[22]	3D finite volume.	None.	Pressure field and cement displacement near the centralizer.
[23,24]	2D Lattice–Boltzmann.	Fluids are treated as particles moving and colliding.	Velocity profile of the annular two-phase flow.

## 2. Cement Displacement Analysis under the Uniform Wellbore Assumption

The process of mud displacement and cement placement involves both single- and two-phase flows in the casing, as well as in the annulus. Here, ‘phase’ refers to a distinct type of fluid, such as mud spacer or cement, rather than a thermodynamic phase like solids, liquids, or gases. To calculate the pressure profile and CDE, it is necessary to model the flow in each well section separately. The results from each section are then combined to form a comprehensive analysis. With increasing wellbore length, the well may comprise more geometrically varied sections. We address this complexity by discussing the application of statistical methods that aim to simplify the model and expedite the analysis.

### 2.1. Problem Statement and Model Partitioning

During the mud displacement process, the casing interior and the annulus together act like a U-tube for fluids. Initially, fluids flow through the casing before entering the annulus. The pressure at the top of the annulus is either atmospheric or regulated by the surface back pressure (SBP) in managed pressure cementing (MPC). To determine the pressure profile and standpipe pressure, we calculate the pressure gradient in both the casing and the annulus. We then integrate these gradients along the casing and annulus to obtain a complete pressure profile.

The flow in the annulus is influenced by the flow rate, fluid rheology, and the geometry of the annulus. In deviated or horizontal wellbores, the casing tends to be displaced towards the lower side of the hole due to gravity, buoyancy, and elasticity/stiffness, even when centralizers are used. As a result, the annulus usually has an eccentric shape. Eccentricity in the annulus, denoted as  $\epsilon$ , is defined by the distance between the casing’s axis and the wellbore’s axis, divided by the gap between them. The annular eccentricity is given by:

$$\epsilon = \frac{D_{\text{wellbore}} - D_{\text{centralizer}}}{D_{\text{wellbore}} - D_{\text{casing}}} \quad (1)$$

where  $D_{\text{wellbore}}$  is the wellbore diameter,  $D_{\text{casing}} < D_{\text{wellbore}}$  is the casing outer diameter, and  $D_{\text{centralizer}} \leq D_{\text{wellbore}}$  is the outer diameter of the centralizer.  $\epsilon = 0$  when  $D_{\text{centralizer}} > D_{\text{wellbore}}$ .

The wellbore diameter is variable, and the casing's relative position changes due to complex loads. Therefore, the annulus' eccentricity varies along the wellbore and its measured depth.

To analyze flow in a wellbore with varying eccentricity, a clear strategy is to first divide the wellbore into multiple segments. We then model and simulate each segment individually. During each operational period, characterized by specific flow rates and casing rotations, we determine the flow model. In segments where cement displaces another fluid, such as mud or spacer, we use a two-phase flow model. In other segments, we apply a single-phase model to simplify and accelerate the simulation. The methodology for modeling annular flow in each segment is detailed in the following section.

With this strategy, the total modeling simulation time is approximately proportional to the total number of sections. The computation of such a detailed model that consists of hundreds or thousands of segments may take weeks or months, which is practically undesirable. Procedures need to be taken to decrease the number of simulations while minimizing the loss of precision. Enayatpour and van Oort [2] showed that, as the eccentricity increases, the pressure gradient in the annulus decreases, and the CDE changes monotonically. In this work, we assume that the casing in each segment is parallel to the wellbore and the eccentricity  $\epsilon$  is as defined in Equation (1). We also assume the eccentricity in the vertical section to be zero. By proper placement of the section boundary, we can segment the eccentricity while keeping the average pressure gradient the same, and the CDE analysis will tend to be conservative (i.e., biased towards lower values) after segmentation.

To use this segmenting method, another underlying assumption is that the frictional pressure is only a function of the well geometry, the fluid rheology, and the flow rate. When the pump rate changes during the operation, the pressure and flow rate in the well go through a transient process before the steady-state flow is restored in the well, and the flow rate is constant along the wellbore. Thus, the flow in a well segment is dependent on the transient flow in the upstream well segment. In this model, we neglect this transient pressure change when the flow rate changes and assume the steady-state state is immediately achieved. Thus, in all well segments, the mass flow rates at the segment entrances are the same during the same operation step. The flow in adjacent well segments is decoupled, and the flow in each well segment can be modeled separately based on the local geometry and the global flow rate. Further, this strategy enables parallelized simulation of the flow in all well segments. With enough computational resources, the analysis of the entire cement placement operation in the well can be performed within approximately the same time as simulating the flow in one well segment.

The flow in the casing is much simpler than the flow in the annulus. Since the intermixing of the fluids is less of a concern in the casing, a single-phase model would be sufficient to estimate the pressure gradient in the casing for pressure analysis. In current cementing practice, the fluids are often treated as Bingham plastic whenever a Newtonian model is determined to be insufficient. Assuming steady-state laminar flow, the velocity profile of a Bingham plastic in the cross-section of a circular casing in the cylindrical coordinate system is given by Dixon [25]:

$$u(r, z) = \frac{1}{4k} \frac{dp}{dz} \cdot (R^2 - r^2) + \frac{\tau_0}{k} (r - R), r > 2\tau_0 / \frac{dp}{dz} \quad (2)$$

where the pressure  $p$  is a function of the radial coordinate  $r$  and the measured depth  $z$ ,  $R$  is the casing inner diameter,  $\tau_0$  is the yield point, and  $k$  is the plastic viscosity.

### 2.2. 3D Modeling of Yield-Power-Law Fluid in Casing and Annulus

Although the rheological behavior of cementing fluids can often be approximated as following the Bingham plastic model in drilling practice, the yield power law or Herschel–

Bulkley model is commonly used when developing cement displacement models and solvers. We have the following:

$$\tau = \tau_0 + k\dot{\gamma}^n \quad (3)$$

where  $\tau$  is the shear stress,  $\dot{\gamma}$  is the shear rate,  $\tau_0$  is the yield stress,  $k$  is the consistency index, and  $n$  is the flow index. When  $n = 1$ , the fluid behaves as a Bingham plastic.

The cement slurry is usually protected by the top and bottom plugs from contamination of the mud while flowing down the casing. Thus, the casing flow is essentially a single-phase flow. The pressure gradient of a yield-power-law fluid in a circular pipe of diameter  $D$  flow, at an average velocity  $V$ , can be numerically solved using the method described by Chilton and Stainsby [26]:

$$\frac{\Delta P}{L} = \frac{4k}{D} \left( \frac{8V}{D} \right)^n \left( \frac{3n+1}{4n} \right)^n \left( \frac{1}{1-X} \right) \left( \frac{1}{1-aX-bX^2-cX^3} \right)^n \quad (4)$$

where

$$X = \frac{4\tau_0}{D} \bigg/ \frac{\Delta P}{L} \quad (5)$$

$$a = \frac{1}{2n+1}; b = \frac{2n}{(n+1)(2n+1)}; c = \frac{2n^2}{(n+1)(2n+1)} \quad (6)$$

In this paper, we apply the 3D submodel for single- and two-phase annular flow as described by Enayatpour and van Oort [2]. This submodel was programmed using the Ansys Fluent 2021R2 software. For more comprehensive details on the model, readers are referred to Enayatpour and van Oort [2], with a concise summary provided in Appendix A.

### 2.3. Casing Connections Modeling

Casing connections link casing sections, creating a continuous barrier against formation fluids. The casing connection can vary in type (threaded coupling, integral, weld-on) and dimensions to enhance its mechanical strength and sealing ability. Different vendors offer casing connections of various inner and outer diameters with different lengths.

The effect of casing connections on mud displacement modeling is not negligible and needs to be considered explicitly to arrive at accurate pressure predictions. Each casing connection is treated as a short section in the casing, assuming the impact of the edges of the casing connection to be negligible. The flow inside the casing connection can be analytically determined, and the annulus flow can be modeled using the methods described in the previous section.

After computing the pressure gradient inside and outside the casing connections, the length-weighted average of the frictional pressure gradient in the pipe and annulus can be calculated. The average frictional pressure gradient is used in the final integration of the results.

### 2.4. Model Validation

Detailed validations of the submodel can be found in Enayatpour and van Oort [2]. This validated submodel is used to establish a model of the flow in the entire well to arrive at a holistic estimate of cement placement. A quick validation of the single-phase flow model against the analytical solution (Bingham plastic) in a circular pipe (Equation (2)) is shown in Figure 1. The inlet mass flow rate is  $3.0891 \times 10^{-5}$  kg/s and the average axial velocity is 0.3933 m/s. The pipe radius is 0.005 m, the fluid yield point is 15 Pa, the consistency index is 0.05 Pa·s, and the fluid density is 1000 kg/m<sup>3</sup>. The analytically calculated pressure gradient is  $1.414 \times 10^4$  Pa/m.

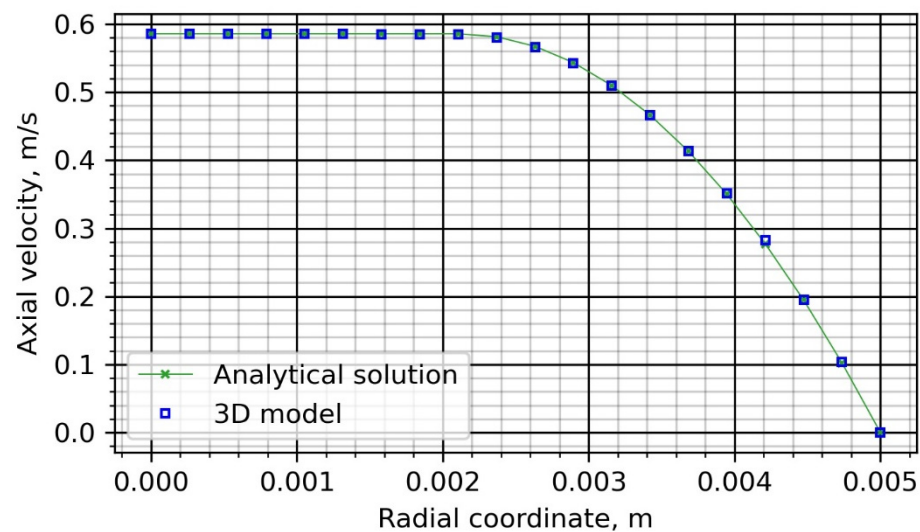


**Figure 1.** Validation of the single-phase flow in a circular pipe. The simulated axial velocity matches the analytical solution.

### 2.5. Result Integration and Entire Displacement Analysis Process

The entire analysis process is elucidated in Figure 2. Firstly, data from the well, the casing, the fluids, and the cement placement operation are loaded as inputs. The well geometry can be from measured or designed directional surveys or from simulation results from a drilling model [27]. Secondly, the location of each fluid in the well is determined by the geometry information and the operation settings, especially the pump rate. The fluid interfaces during the displacement operation are tracked to find the critical time frames when any fluid interface reaches any well section boundary and when the flow rate changes. In estimating the front of the cement, we assume a negligible impact from an un-displaced spacer, valid mainly when the CDE is close to 100%. At lower CDEs, the cement–spacer interface propagates faster, altering the critical time frames. The wellbore is then segmented as outlined in the model partitioning section. Thirdly, a 3D transient finite volume model of single- or two-phase flow is established and simulated for each annular well segment. This step is based on the previous work [2], and no modification was made to the modeling in each section. The frictional pressure in each casing section is either simulated in the same way as in the annulus or, if it is single-phase Bingham plastic, is analytically calculated. Finally, the CDE is determined at the cement front position in the annulus, and the pressure is calculated by summing up pressure drop across all downstream pipe and annular well segments, using Bernoulli’s equation.

All the input variables involved in the proposed model are listed in Figure 3. Although not marked separately, the system may have several wellbore sections, several casing sections, and several fluids. Associated with each of these elements will be a separate input data set with variables, as shown in Figure 3. The well trajectory can be the designed trajectory, the measured survey, or the simulation results from a numerical model [27]. When a wellbore caliper log is available, or the distribution of the wellbore diameter can be inferred from historical data (e.g., acoustic pseudo-caliper obtained during drilling), it is possible to break the wellbore into hundreds or thousands of segments for very precise analysis. However, performing such a detailed level of analysis within a reasonable time will require more advanced and optimized modeling following, e.g., a data-based approach, a topic that is beyond the scope of this paper. To decrease the computational expense, a straightforward idea is to average the wellbore diameter in a relatively long well segment and assume the flow in the segment can be approximated by the flow in the well of the averaged geometry. To justify this practice of averaging the wellbore diameter, Appendix B examines the wellbore diameter distribution of a well segment, and Appendix C analyzes the impact of the wellbore diameter distribution on the pressure gradient analysis using the

model in this work. In this paper, we break down the well into a few long well segments, assume the wellbore diameter in each well segment follows its own distributions, and use the average wellbore diameter in each well segment for the flow analysis.

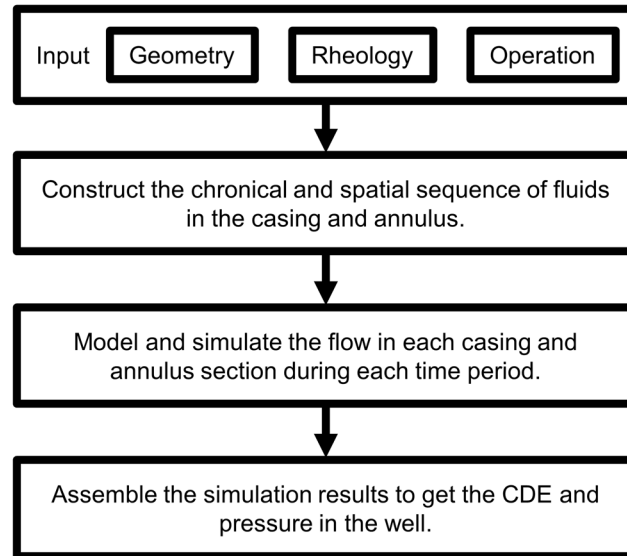


**Figure 2.** Workflow of cement placement/mud displacement analysis. The chronological and spatial sequence of the fluids is established based on the geometry and operation parameters. The flow in each section in the casing and annulus is modeled and simulated before being integrated into the final results of CDE and pressure.

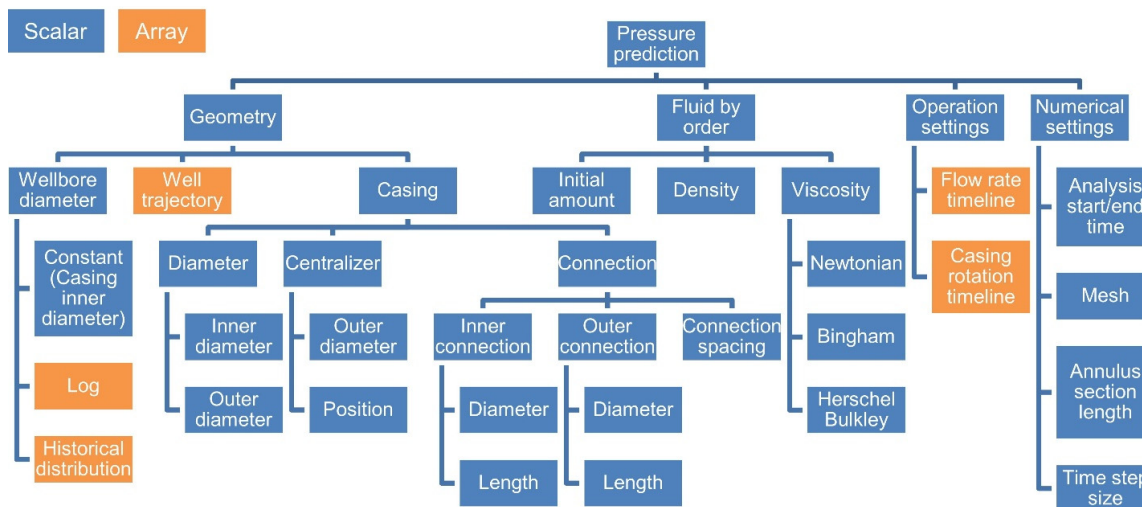


**Figure 3.** Data inputs involved in modeling the mud displacement/cement placement operation.

The modeling of the single- and two-phase flow in a wellbore segment was discussed in the previous section. Although the model is transient, steady-state pressure and CDE are used for the analysis. After modeling and simulating the flow in each wellbore segment, the pressure and the CDE are post-processed separately.

The pressure gradient in each wellbore segment indicates the associated frictional pressure loss in that segment. We integrate this pressure gradient along the casing and the annulus to obtain the total frictional pressure loss in the well. Combining the frictional pressure loss and the total gravity yields the surface pressure. This assumes no MPC surface back pressure management (if MPC is used, that back pressure can be straightforwardly added to the surface pressure). The pressure is analyzed at every critical time frame, as defined at the beginning of this section. The pressure between these critical time frames is linearly interpolated.

The CDE in each wellbore segment is correlated with the position of the cement front. As the mud displacement operation continues, the cement front advances in the annulus. In each segment in the annulus, the geometry is constant or averaged, as discussed in Appendices B and C; thus, the CDE is constant at a constant flow rate.

### 3. Field Case Study

We applied our proposed modeling method to a horizontal well's cementing operations, which faced unexpectedly high surface pressure during a slim-hole cement job. Firstly, the impact of several factors on the surface pressure was evaluated. Then, the surface pressure and CDE were analyzed based on pre-job and post-job data with a constant wellbore diameter assumption for the well (referred to in the following as Well X). Finally, we incorporate the wellbore diameter obtained from ultrasonic borehole diameter measurement and the impact of the mud viscosity to demonstrate the impact of these parameters and the accuracy of our modeling method.

#### 3.1. Case Introduction

Well X was an actual horizontal well of typical L-shape geometry and approximately 22,000 ft measured depth. The kick-off point (KOP) was at approximately 11,000 ft TVD, and the lateral section started at approximately 12,000 ft TVD. The schematic and trajectory in accordance with the well survey of Well X are shown in Figure 4. Based on the concept of segmentation, the entire annulus was broken into three segments, and the pressure fluctuation caused by non-constant wellbore diameter was assumed to average out. The vertical section was drilled in the previous operation steps, and the inner diameter of the previous intermediate casing string was 6.969 in. The planned average borehole diameter was 6.75 in. below 11,000 ft TVD. The wellbore diameter distribution of a section of the well acquired from the ultrasonic measurement data is shown in Appendix B. However, in this paper, we base the analysis on the average wellbore diameter because the analysis in Appendix C shows that the relative error between using the average wellbore diameter and the real wellbore diameter is <1%. The production casing had a 5.5 in. outer diameter and a 4.778 in. inner diameter with 6.252 in. centralizers placed at every 44 ft along the casing. Based on the wellbore and casing properties, the typical annulus eccentricity was 0.3–0.4. The measured bottom hole static temperature (BHST) was 168.2 °F.

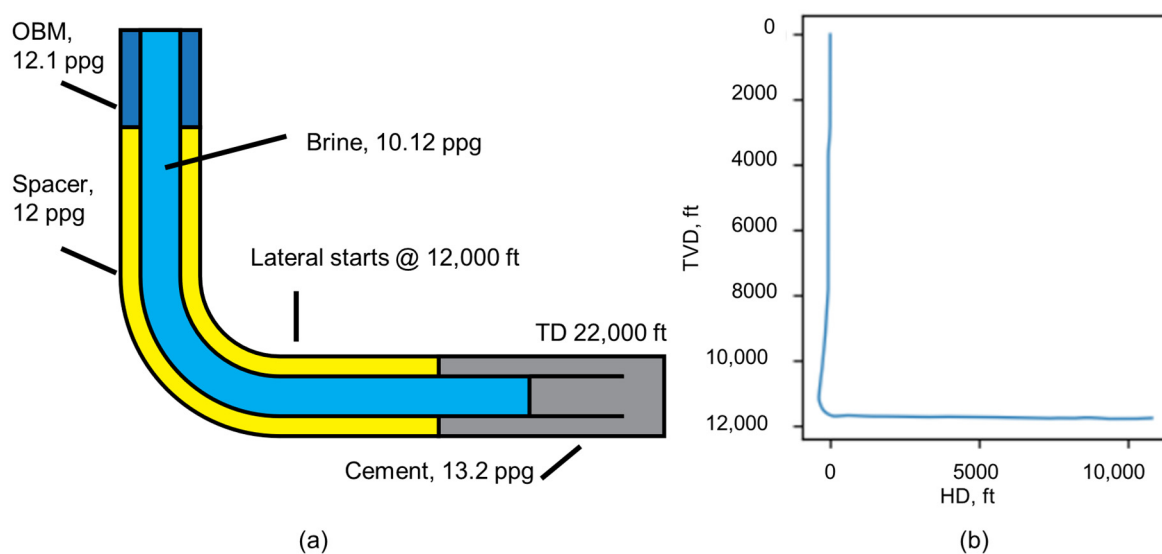


**Figure 4.** (a) Schematic of Well X, with a snapshot of a moment during the displacement. Colors: light blue—brine; grey—cement; yellow—spacer; dark blue—mud. The fluid densities are marked in the figure, and additional fluid properties are included in Table 2. (b) 2D trajectory of Well X (side view), true vertical depth (TVD) vs. horizontal displacement (HD).

Table 2. Fluid properties.

Fluid	Density, ppg	Density, kg/m <sup>3</sup>	Consistency Index $k$ (Plastic Viscosity, PV), cP	Yield Pressure (YP) $\tau_0$ , Pa	Measurement Temperature, °F
OBM	12.1	1450	17	5.27	150
Spacer	12.0	1438	16.3	7.56	168
Cement	13.2	1582	60.7	4.42	168
Brine	10.1	1213	1.0	0.96	120

Before the cement operation started, both casing and annular spaces were filled with oil-based mud (OBM). Then, the fluids were pumped into the casing in the order of spacer, cement, and brine. The properties of the fluids (mud, spacer, cement, brine) used in the case study analysis are from the cementing job report and are listed in Table 2. Although the model is designed for a more generalized yield-power-law fluid, the Bingham plastic fluid is easily modeled by setting the flow index to  $n = 1$ , as mentioned in Section 2.2. Note that the reported OBM viscosity was measured at 150 °F, not 168 °F.

Figure 5 shows the planned (dash lines) and actual (solid lines) pump rate and surface pressure during the entire cement displacing operation. The entire cement displacement operation consisted of the following steps.

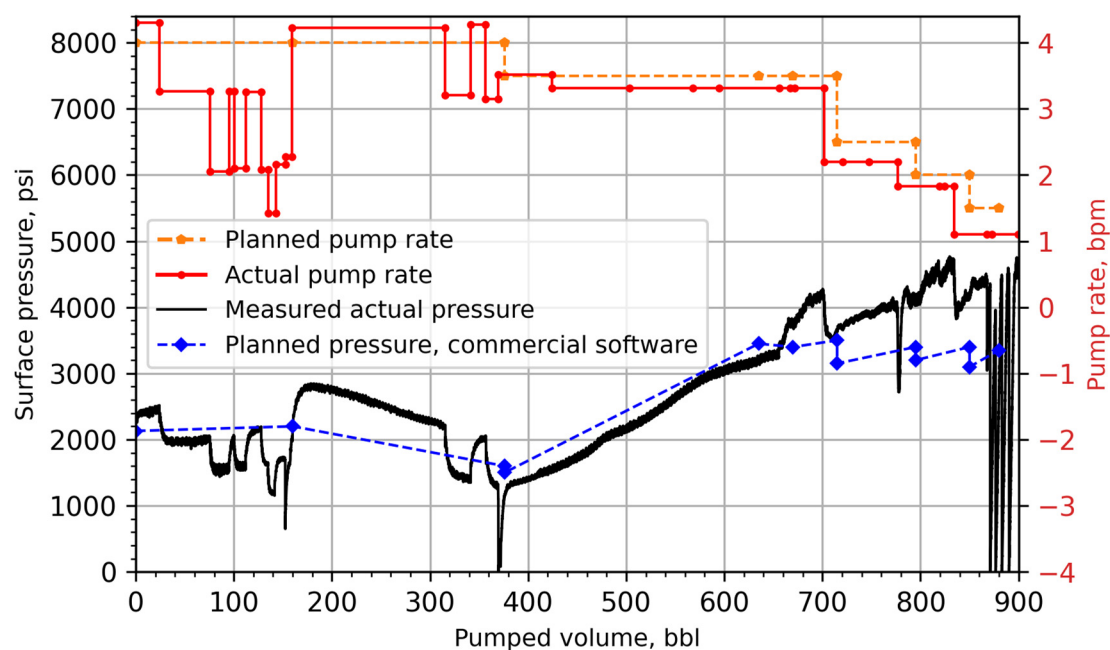


Figure 5. Planned (dash line) and actual (solid line) pump rate and surface pressure at different pumped volumes during the displacement. Note the discrepancy between actual pressure (green solid line) and planned pressure (blue dashed line).

Step 1: from 0 bbl to 375 bbl displacement, the spacer and the cement were pumped. Although a constant flow rate of 4.0 bpm was planned, the actual pump rate fluctuated between 1.4 bpm and 4.3 bpm. From 25 bbl to 160 bbl displacement, the actual pump rate was 17–65% lower than the planned pump rate. The actual surface pressure was only 0–32% lower than the planned pump pressure. However, from 160 bbl to 310 bbl, when the actual pump rate was only 5% higher than the planned pump rate, the actual surface pressure was 33% higher than the planned surface pressure. Multiple pauses (0–20 min) were made for various operations after 310 bbl displacement. At 375 bbl displacement, the pump was stopped, and the top plug was dropped. Operations in this step lasted for less than half an hour.

Step 2: from 375 bbl to 700 bbl displacement, the displacement brine was pumped. Because of the higher-than-expected pressure during 0–425 bbl displacement, the flow rate was decreased by 0.2 bpm from 3.5 bpm to 3.3 bpm after 425 bbl displacement. The spacer front reached the bottom hole at 500 bbl displacement volume. The estimated bottom hole circulating temperature (BHCT) during this time was 167.8 °F in the plan, and the surface pressure estimation used the OBM viscosity at 167.8 °F, which was not provided in the design report. At 650 bbl displacement, the actual surface pressure sharply increased while the planned surface pressure gradually decreased. The surface pressure peaked (4277 psi) at 700 bbl displacement and was 22% higher than the planned maximum surface pressure of 3500 psi, leading to a pause in the operation.

Step 3: after 700 bbl displacement, the pump rate was decreased (initially by 0.3 bpm and then more) from the planned value to keep the pressure within the limits of the surface system. However, higher surface pressure, even at the lowered pump rates, was seen. In the absence of sufficient data to directly reveal the cause, one possible hypothesis is that the cement gelled during the longer pumping time due to the lower pump rate and the pause. At 840 bbl displacement, the pressure exceeded 4000 psi again. The operation was paused, and a pressure test was performed. The operation continued after the pause at progressively lowered pump rates and even higher surface pressure.

During Step 1, the actual surface pressure was considerably higher than anticipated. In Step 2, the peak surface pressure reached 4277 psi at 700 bbl, nearing the upper limit (4500 psi) of the pressure test, jeopardizing safety and system integrity, leading to operational pauses and non-productive time (NPT). Notably, at 650 bbl displacement, there was a sharp increase in surface pressure, contrary to the expected gradual decrease. This study is independent of that of the service company, and it is unknown what modeling approach was used or what assumptions were made that led to the evident discrepancy in peak surface pressure. The differences between planned and actual pressures, as shown in Figure 5, highlight the need for improved analysis methods. Precise pressure analysis for slim-hole cement placement operations is crucial to avoid future incidents of excessive surface pressure, associated risks, and NPT.

### 3.2. Factors Influencing Surface Pressure

To understand the displacement process, we first study the influence of several factors on the frictional pressure.

During mud and spacer displacement, the pump rate is reduced to prevent turbulent flow in the annulus and to improve the stability of the cement–spacer interface. This minimizes cement contamination and improves CDE. Thus, the flow is assumed to be laminar. The influence of the pump rate on the laminar flow frictional pressure in the annulus is shown in Figure 6. The fluid properties of the spacer, OBM, and cement are listed in Table 2. The dots are simulation results, and the straight lines are linear fits to the data points. The annular frictional pressure gradient appears to increase linearly with the pump rate for both OBM and spacer. In mud displacement operations, fluid may pass through an annulus section at varying pump rates during different operational stages. This study leverages the linear relationship between the annular frictional pressure gradient and flow rate to streamline and expedite analysis. For single-phase flow cases, we simulate only the case with the smallest and largest flow rates. Other scenarios are interpolated based on this linear relationship for each fluid in every well section. The reduction in the simulation cases varies with the number of operation steps.

The frictional pressure gradient in the annulus increases nonlinearly when the wellbore diameter decreases, as shown in Figure 7. The trend lines are polynomial, and the preliminary result of fitting the pressure gradient data is included in Appendix C. The flow rate, in this case, is 2.2 bpm. The pressure gradient increases rapidly as the wellbore diameter decreases and approaches the casing diameter, closing the already narrow gap. The difference in the frictional pressure gradient between different fluids also increases rapidly when the wellbore diameter decreases. The wellbore diameter is never constant and

may decrease in some well sections because of elevated reservoir pressure and wellbore instability, non-optimum directional drilling practices, etc. When the cement front enters a narrow zone in the annulus, the pressure gradient in the annulus section rapidly increases, leading to a sharp increase in the surface pressure. The pressure–wellbore diameter relationship also impacts the frictional pressure of casings with a casing connection of larger outer diameter. For example, a 5.5 in. casing with a 6.05 in. outer diameter casing connection covering 2% of the length of the casing could give rise to a 3% higher frictional pressure in the annulus than a 5.5 in. casing with a flush connection.

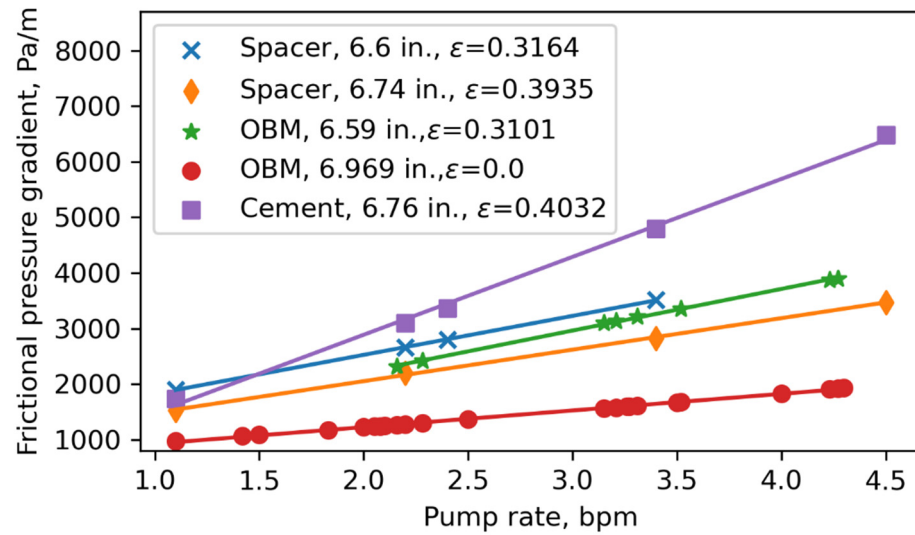


**Figure 6.** Linear relationship between the frictional pressure gradient and the pump rate in the annulus for different fluids at different wellbore diameters and different eccentricities,  $\epsilon$ . The casing outer diameter is 5.5 in. with 6.252 in. outer diameter centralizers with laminar flow in the annulus.

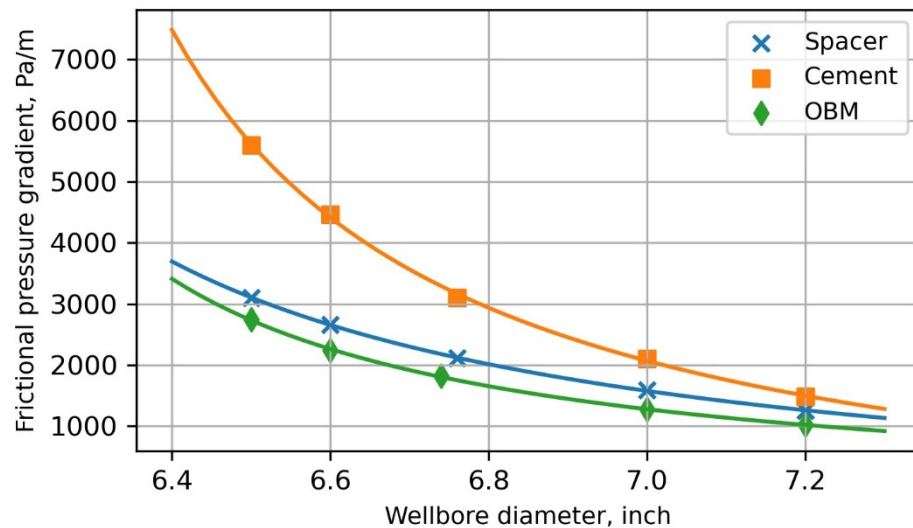


**Figure 7.** Impact of wellbore diameter on the frictional pressure gradient in the annulus. The casing diameter is 5.5 in. with 6.252 in. centralizers. The flow rate is 2.2 bpm.

The frictional pressure gradient in the annulus increases when the plastic viscosity and yield point increase, and vice versa. The frictional pressures of the OBM as a function of plastic viscosity and yield point are shown in Figure 8. When the temperature increases, the plastic viscosity and the yield point of an OBM may decrease sharply [28,29]. Accurate measurement of plastic viscosity and yield point at the correct temperature is crucial for precise pressure analysis during cement displacement. Therefore, accurately

predicting downhole temperature behavior during the cementing job is vital for proper fluid viscosity characterization.

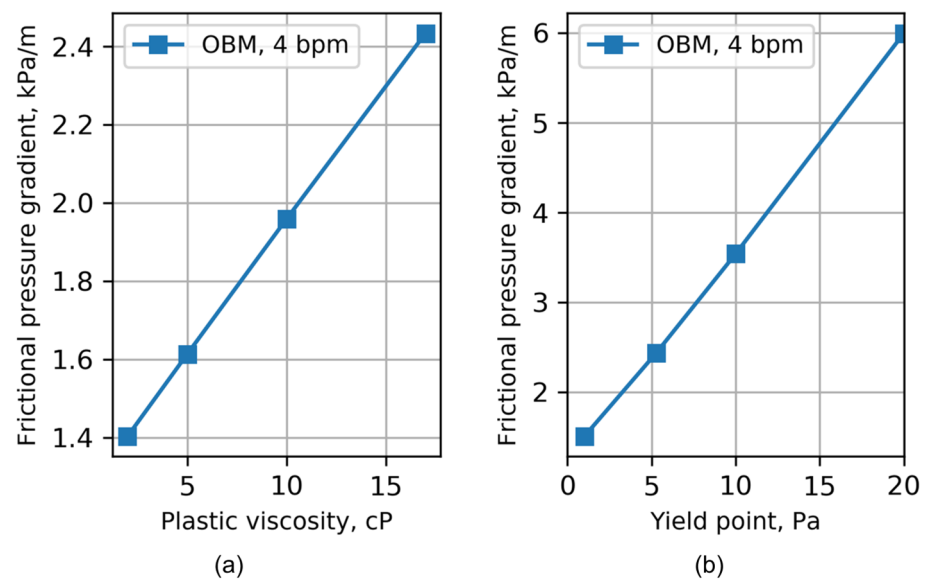


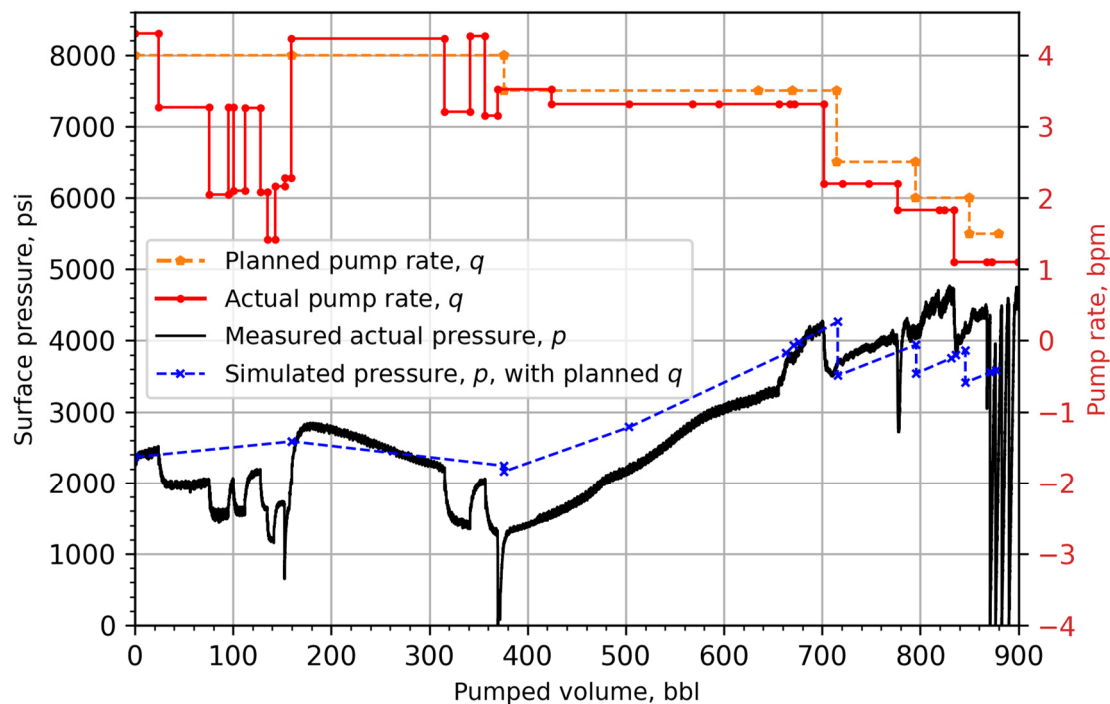
**Figure 8.** Impact of (a) plastic viscosity (with yield point = 5.27 Pa) and (b) yield point (with plastic viscosity = 17 cP) on the frictional pressure gradient in the annulus. The constant yield point is chosen to be 5.27 Pa. The casing diameter is 5.5 in. with 6.252 in. centralizers.

### 3.3. Simulation Results

In this section, we first show the simulated surface pressure based on the planned pump rate, the planned wellbore diameter, the OBM viscosity measured at 150 °F, and the reported cement viscosity, assuming it did not gel during the placement. Then, we successively adjust the pump rate, the OBM viscosity, the wellbore diameter, and the cement viscosity in the model based on data from the post-job report and lab measurements. The surface pressure is simulated based on the adjusted inputs to show the particular influence of the various factors.

Well X had 19 operation steps according to the actual pump rate data. To assess the frictional pressure gradient in each well segment for every operation step, we initially required 140 simulation cases. However, leveraging the linear relationship between pump rate and annular pressure gradient, we reduced the number of simulations to 42. The skipped simulations were effectively estimated using linear interpolation. The simulations were performed on a laptop computer with an Intel i7-4940MX CPU (8 cores at 3.10 GHz). The simulation time for an analysis was less than seven days. The simulation of the flow in each well segment took 0.5–2 h.

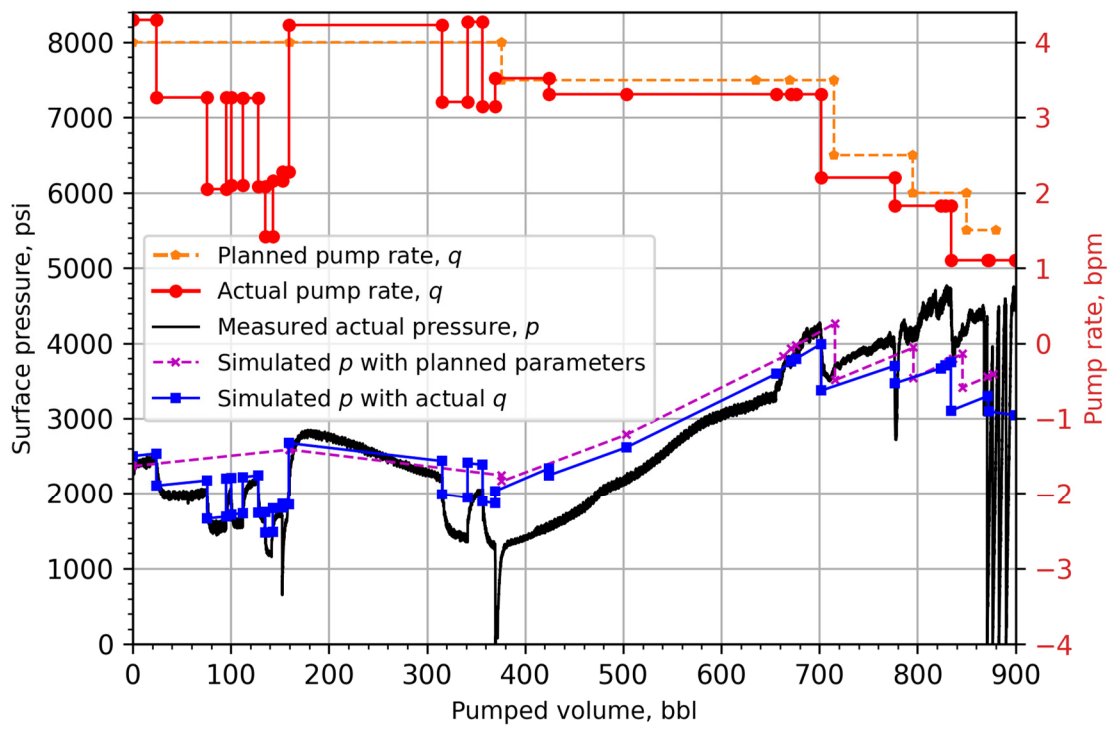
The simulated surface pressure based on the planned data is shown in Figure 9. From 0 bbl to 375 bbl displacement, the simulated pressure is within the 200 psi range from the planned pressure when the actual pump rate is slightly higher than the planned pump rate. From 375 bbl to 715 bbl displacement, the simulated pressure is higher than the actual pressure because the input OBM viscosity was measured at 150 °F, a factor that will be discussed later in this paper. The planned pressure showed a maximum surface pressure of 4264 psi at 715 bbl displacement, which is only 0.3% lower than the measured data of 4277 psi at 700 bbl. The trend of the simulated surface pressure always follows the trend of the actual surface pressure.



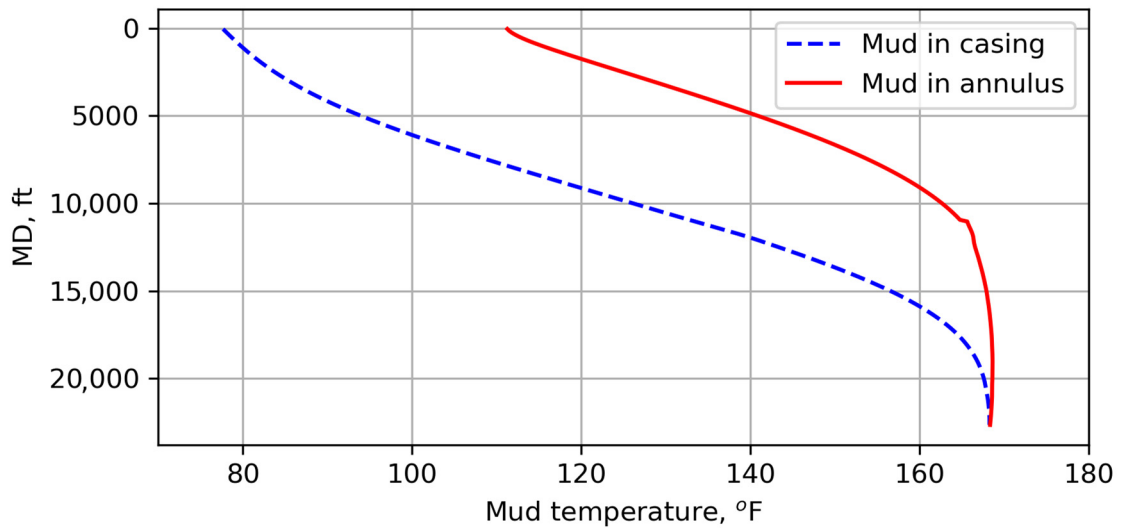
**Figure 9.** Planned (dashed line) and actual (solid line) pump rate,  $q$ , and surface pressure,  $p$ , at different pumped volumes during the displacement. The planned pressure is based on the proposed model and the planned pump rate,  $q$ .

Figure 10 shows the simulated surface pressure based on the actual pump rate. From 0 bbl to 160 bbl displacement, the simulated surface pressure tracked the actual surface pressure with minor errors. The error is mostly caused by the transient pressure fluctuation, which is not considered in this model. The simulated peak surface pressure (3992 psi) at 700 bbl displacement is 6.6% lower than the actual peak surface pressure (4277 psi). The surface pressure decreases when the pump rate increases, meaning that if the actual pump rate had been provided, the results from the commercial software would have further deviated from the actual pressure.

The design report listed the BHCT during cement placement as 167.8 °F. We used a thermal-hydraulics model, as described by Khaled et al. [30,31], to analyze the mud temperature distribution, with the result shown in Figure 11. At a BHCT of 168 °F, the OBM temperature in the lateral section is at least 166 °F, decreasing upon leaving this section. According to Fakoya and Ahmed [32], the OBM viscosity decreases as the temperature increases. Hence, the OBM viscosity measured at 150 °F exceeds that at 168 °F. To estimate the actual OBM viscosity at 168 °F, not provided in the report, we measured the viscosity of a similar OBM at 150–168 °F using a rheometer, as detailed in Table 3. The plastic viscosity of the similar OBM decreased from 29.9 cP to 22.2 cP, while the yield pressure decreased from 12.9 Pa to 11.9 Pa. Based on these measurements, we hypothesize that, in the field case, the OBM plastic viscosity decreased from 17 cP by 7 cP to 10 cP during the cement placement and then increased back to 17 cP, with an assumption of a constant yield point of 5.27 Pa for simplicity. This approximation seems reasonable, considering the similar impacts of the yield point and the plastic viscosity on the frictional pressure, as illustrated in Figure 8. Figure 12 shows the surface pressure with the adjusted OBM viscosity. With the OBM viscosity corrected, the simulated surface pressure matches the actual surface pressure in most parts in the 0 bbl to 700 bbl displacement interval. The surface pressure at 370 bbl displacement is lowered by 400 psi by the correction of the viscosity. The results from the commercial software are already based on the OBM viscosity measured at 168 °F; therefore, it could not be further improved by the correction of viscosity.



**Figure 10.** Simulated and actual pump rate,  $q$ , and surface pressure,  $p$ , at different pumped volumes during the displacement. The simulated pressure is based on the proposed model and the actual pump rate,  $q$ .



**Figure 11.** Mud temperature in the well during the cement placement after 380 bbl displacement. The BHCT is 168 °F.

**Table 3.** OBM viscosity.

Temperature, °F	Plastic Viscosity, cP	Yield Point, Pa
150	29.9	12.9
160	25.7	12.3
168	22.2	11.9

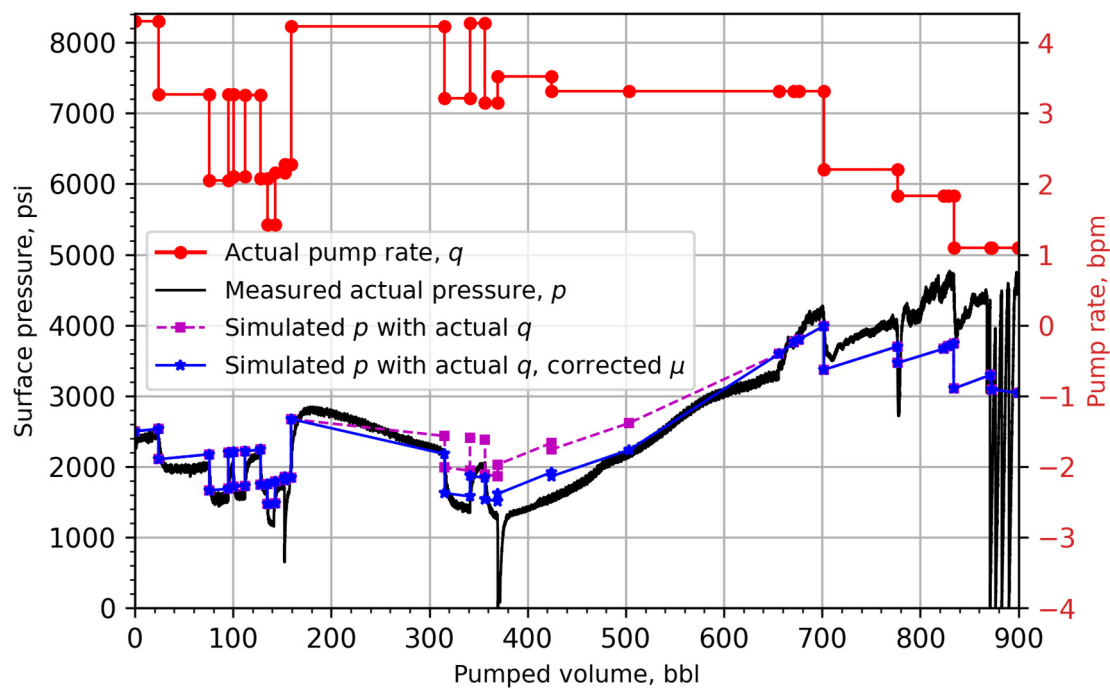


**Figure 12.** Simulated and actual pump rate,  $q$ , and surface pressure,  $p$ , at different pumped volumes during the displacement. The simulated pressure is based on the proposed model, the actual pump rate,  $q$ , and the corrected OBM viscosity,  $\mu$ .

Figures 11 and 12 highlight the importance of considering the impact of temperature in the model. We introduce a one-way coupling strategy, as described at the end of Appendix C, to incorporate the impact of temperature on the viscosity.

Contrary to the initial assumption of a uniform 6.75 in. wellbore, ultrasonic borehole diameter measurements revealed an average wellbore diameter of only 6.58 in. between 16,200 ft and 18,300 ft. Figure 7 demonstrates that the frictional pressure grows nonlinearly when the annulus outer diameter (the wellbore diameter) decreases. When the spacer and the cement enter the narrow zone of the annulus, the total frictional force in the narrow zone also changes nonlinearly, resulting in a sharp increase in the surface pressure. The surface pressure with the adjusted wellbore diameter is shown in Figure 13. The overall surface pressure is increased by the narrower wellbore section, and the sharp increase at 650 bbl displacement is matched. The simulated peak surface pressure (4046 psi) at 700 bbl displacement is 5.4% lower than the actual peak surface pressure (4277 psi). The overall influence of the narrow section on the surface pressure is marginal. Thus, the results from the commercial software would not improve significantly even with the use of the measured wellbore diameter in the simulation.

In the absence of cement measurement data, we conducted an analysis of the abnormally high pressure after 700 bbl displacement. In Figure 13, it is shown that the actual surface pressure sharply increased even at a decreased pump rate after 700 bbl displacement. A plausible hypothesis is the gelling of the cement. We assumed an increase in the cement plastic viscosity to 120.7 cP for this analysis, with the simulated surface pressure shown in Figure 14. The trend in the simulated surface pressure closely aligns with the actual pressure trend, and the peak simulated surface pressure (4722 psi) at 830 bbl displacement is only 0.08% lower than the actual peak simulated surface pressure (4726 psi). This close match under the mud gelation hypothesis suggests it is a likely root cause. However, the exact reason for the unusual high pressure after 700 bbl remains uncertain due to the lack of direct cement measurement data.

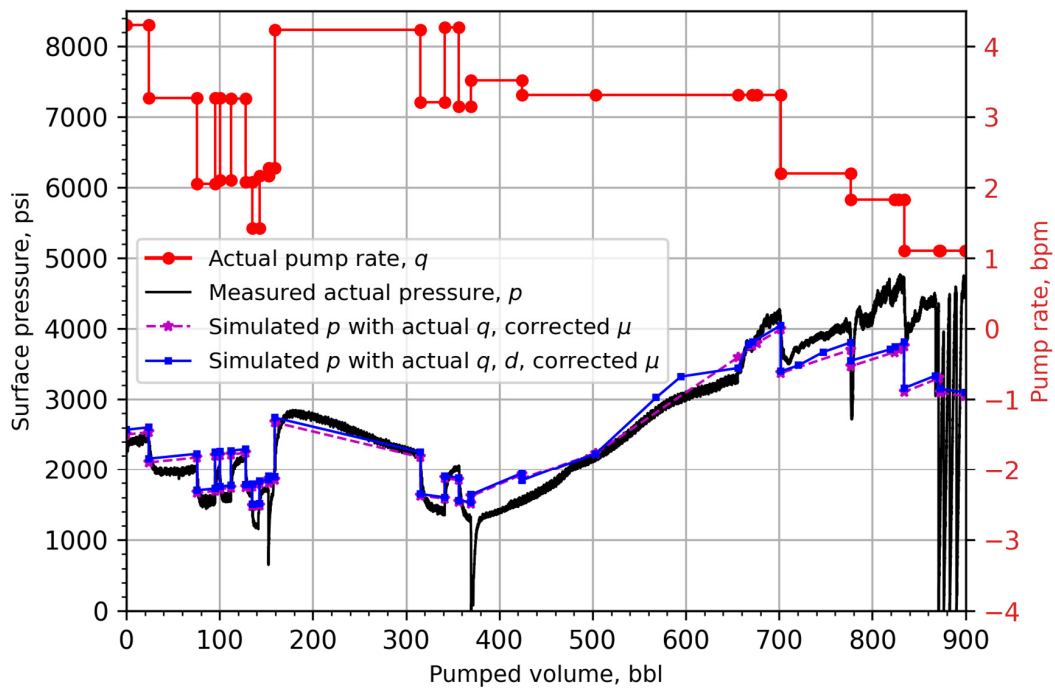


**Figure 13.** Simulated and actual pump rate,  $q$ , and surface pressure,  $p$ , at different pumped volumes during the displacement. The simulated pressure is based on the proposed model, the actual pump rate,  $q$ , the actual wellbore diameter,  $d$ , and the corrected OBM viscosity,  $\mu$ .

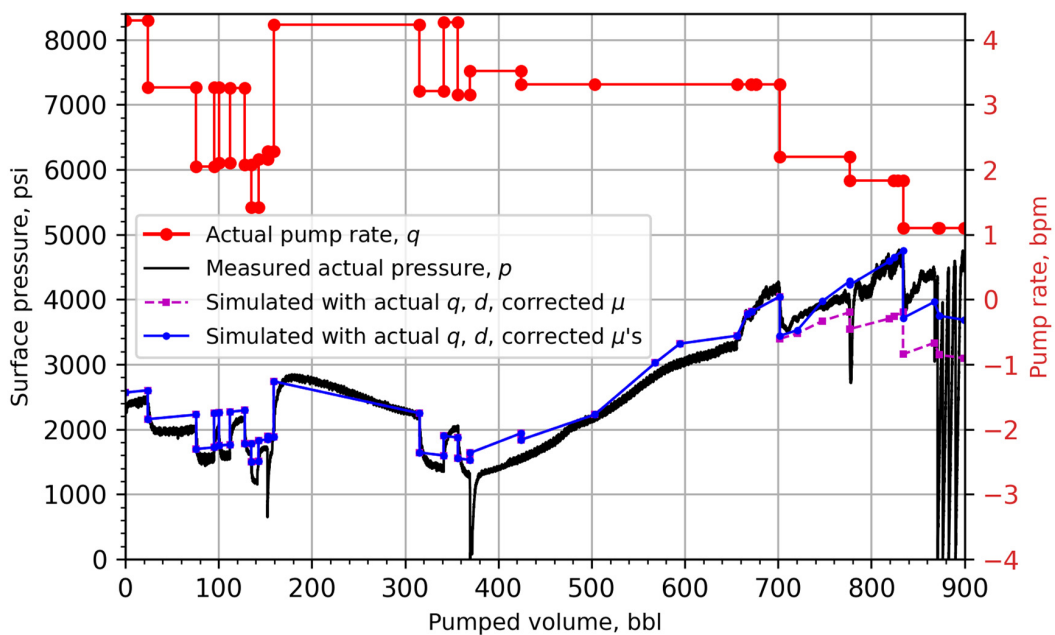


**Figure 14.** Simulated and actual pump rate,  $q$ , and surface pressure,  $p$ , at different pumped volumes during the displacement. The simulated pressures are based on the proposed model, the actual pump rate,  $q$ , the actual wellbore diameter,  $d$ , the corrected OBM, and original and corrected cement viscosity,  $\mu$ 's.

Finally, Figure 15 illustrates the combined impact of four key factors: pump rate, wellbore diameter, OBM viscosity, and cement viscosity. By adjusting these four factors based on field and lab data, we significantly reduced the discrepancy between the simulated and actual surface pressures. Figure 15 demonstrates that, with precise inputs, our model provides an accurate estimation of the surface pressure, especially the peak surface pressure.

Despite uncertainties in these parameters, the model’s peak surface pressure estimation is remarkably accurate, with an error of  $\leq 6.6\%$ . Results with this accuracy can be used to better select operational equipment and cement job parameters and manage the cement job in the field. Conversely, from 0 bbl to 700 bbl displacement, the results from the commercial software would not be significantly improved and might even deteriorate by adjusting the inputs of the pump rate, wellbore diameter, and OBM viscosity.

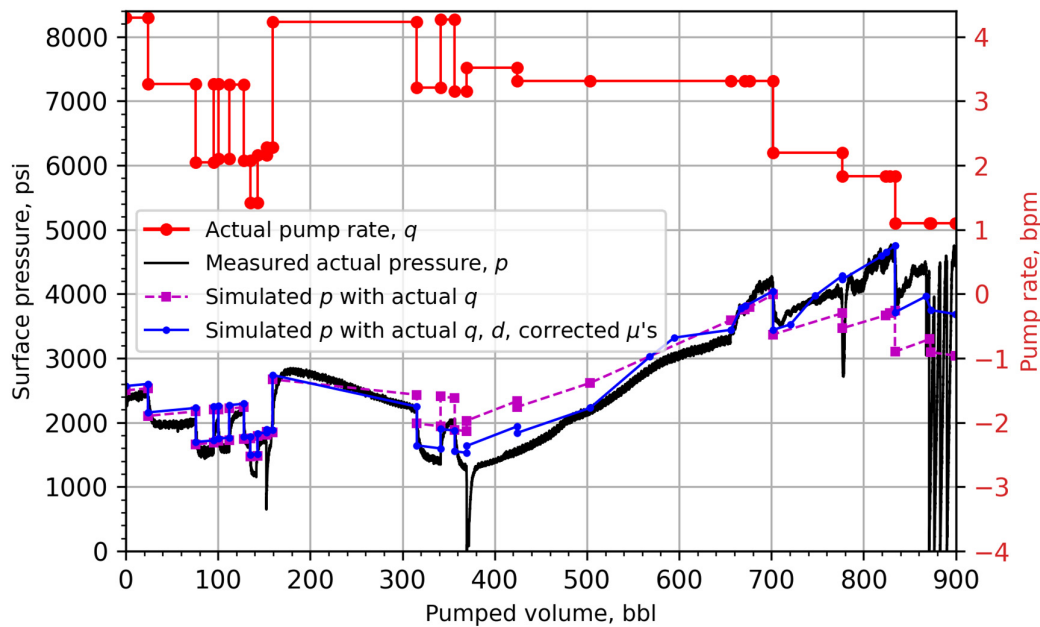


**Figure 15.** Simulated and actual pump rate,  $q$ , and surface pressure,  $p$ , at different pumped volumes during the displacement. The simulated pressure is based on the proposed model, the actual pump rate,  $q$ , the actual wellbore diameter,  $d$ , and the corrected OBM and cement viscosity,  $\mu's$ .

The simulated CDE based on the planned and actual data is shown in Figure 16. Notably, the CDE simulations, with or without the adjustments mentioned earlier, show no significant observable differences. In every operational step, both the planned and actual CDEs exceed 99%, signaling a successful mud displacement and cement placement operation. No cement quality issue was reported after the cement job, which is in indirect agreement with the CDE analysis.

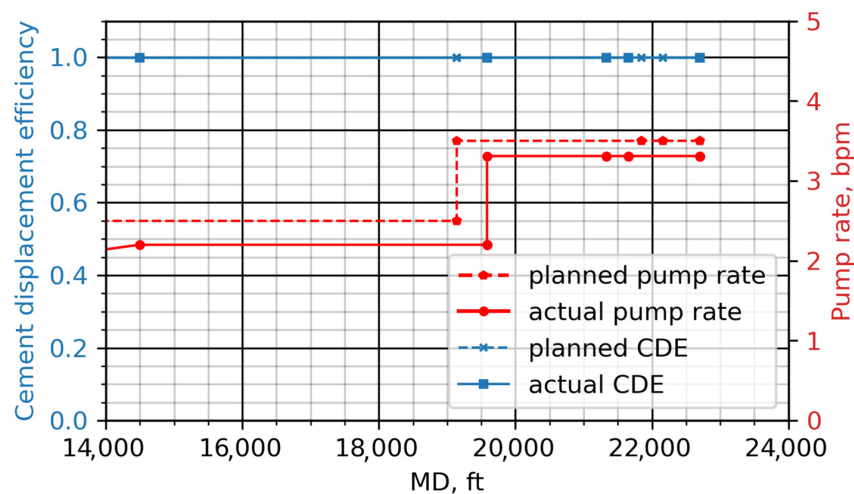


**Figure 16.** Planned (dash lines) and actual (solid lines) CDE when the cement front reaches each MD. The planned and actual CDE curves are both very close to the CDE = 1.0 grid line.

#### 4. Conclusions

This paper documents the development of a high-precision 3D model for the entire mud displacement and cement placement operation during slim-hole casing cementation. This model is based on high-precision 3D flow consideration in short well segments. The modeling software used is Ansys Fluent 2021R2, a trusted commercial CFD solver that has been used in various industrial fields for many years. The model allows for pressure and CDE analysis during the entire operation within a modeling timeframe of a week on a regular laptop computer. This analysis time can be reduced to less than a few hours when using a high-performance computer, by using multiple standalone computers in parallel, or by using a data-driven machine learning approach (see “Guidance for future work” below). The main conclusions are the following:

1. The model was validated with a slim-hole cementing field case study for an unconventional shale well. It showed a marked improvement in predicting the trend and absolute peak value of the surface pressure with an acceptable precision (showing only 0.3–5.4% error), particularly when compared to the results of a commercial software model used in the field (showing 18.2% error).
2. A linear relationship between the flow rate and the frictional pressure gradient was used to calculate the frictional pressure gradient based on the data of the same fluid in the same well section at different flow rates. This linear interpolation method decreased the required number of simulation cases from 140 to 42, i.e., a 70% reduction with an associated reduction in simulation time.
3. Accurate casing and wellbore geometry estimation and fluid viscosity measurement were found to be of pivotal importance to obtaining correct pressure values. An average wellbore diameter was adopted to model the pressure gradient in each well section, noting that an analysis that explicitly considered the wellbore diameter distribution offered only a marginal improvement in accuracy.

This paper lays a foundation for better slim-hole cementing through improved modeling of pressure and CDE in narrow annuli. Such modeling will help to avoid exceeding pressure limits and having to make unanticipated adjustments during the actual job itself that may jeopardize the success of the entire cementing operation. The modeling and simulation method and associated workflow have been automated, thereby opening up an avenue for fully automatic cementing job design.

#### 5. Guidance for Future Work

A few future work efforts are recommended to improve the accuracy of the analysis presented in this paper. To better consider the impact of temperature on fluid (mud, spacer) and cement viscosities and thereby improve the pressure estimation accuracy, a temperature model can be two-way coupled with the 3D hydraulic model described in this work. In addition, the impact of the wellbore diameter distribution on the pressure analysis accuracy is still unclear. The criteria to determine the distribution function that best represents the wellbore diameter can be further explored. For wells with irregular cross-sectional shapes, the proper representation of wellbore geometry can be studied further.

High CDE is essential for a successful cementing job. If the CDE is predicted to be significantly lower than 100%, the cementing job should be redesigned and optimized. However, when conducting pressure analysis in such cases, it is important to account for the fact that the cement front travels faster than the cases discussed in this paper, and the fluid interface tracking must consider the impact of CDE.

The lower limit of the running time of the cement placement analysis method is the simulation time of the flow in a well segment. To further accelerate the analysis and reduce simulation run-time, a data-driven machine learning approach may prove beneficial. This is expected to reduce analysis time from days and weeks to only hours and minutes on a standard computer laptop.

**Author Contributions:** Methodology, N.W.; software, N.W.; validation, N.W.; formal analysis, N.W.; investigation, C.L.; resources, G.G. and T.G.; data curation, G.G. and T.G.; writing—original draft, N.W.; writing—review and editing, C.L., P.A. and E.v.O.; visualization, N.W.; supervision, P.A. and E.v.O.; project administration, P.A. and E.v.O.; funding acquisition, E.v.O. All authors have read and agreed to the published version of the manuscript.

**Funding:** The RAPID (Rig Automation and Performance in Drilling) Industry Affiliate Program (IAP) at UT Austin is thanked for the financial support and technical guidance of this project.

**Data Availability Statement:** Restrictions apply to the availability of these data. Data were obtained from Occidental and are available from the authors with the permission of Occidental.

**Acknowledgments:** The authors want to thank Ivan Feng for the OBM viscosity measurements. Occidental is thanked for permission to publish this paper.

**Conflicts of Interest:** Authors Garrett Granier and Tatiana Gobert were employed by the company Occidental. The remaining authors declare that the research was conducted in the absence of any commercial or financial relationships that could be construed as a potential conflict of interest.

## Nomenclature

BHA	Bottom hole assembly
BHCT	Bottom hole circulating temperature
BHST	Bottom hole static temperature
CDE	Cement displacement efficiency
$\epsilon$	Annular eccentricity
HD	Horizontal displacement
KOP	Kick-off point
MAPE	Mean absolute percentage error
MLE	Maximum likelihood estimation
MPC	Managed pressure cementing
NPT	Non-productive time
OBM	Oil-based mud
PDF	Probability density function
SBP	Surface back pressure
SSE	Sum squared error
TD	Total depth
TVD	True vertical depth
VOF	Volume of fluid

## Appendix A. 3D Modeling of Two-Phase Flow in the Annulus

For both the single- and two-phase flows, transient models are based on the continuity equation given by:

$$\frac{\partial \rho}{\partial t} + \nabla \cdot (\rho \vec{u}) = S_m \quad (\text{A1})$$

where  $\rho$  is the density,  $\vec{u}$  is the fluid velocity, and  $S_m$  is the source term added to the continuous phase from the element boundaries or from any dispersed phase inside the continuous phase. For incompressible fluids, the continuity equation becomes:

$$\nabla \cdot \vec{u} = 0 \quad (\text{A2})$$

The momentum conservation equation is given by:

$$\frac{\partial \rho \vec{u}}{\partial t} + \nabla \cdot (\rho \vec{u} \vec{u}) = -\nabla p + \nabla \cdot (\bar{\tau}) + \rho \vec{g} + \vec{F} \quad (\text{A3})$$

where  $p$  is the pressure,  $\vec{g}$  is the gravity,  $\vec{F}$  is the external body load, and  $\bar{\tau}$  is the stress tensor given by:

$$\bar{\tau} = \mu \left[ \nabla \vec{u} + (\nabla \vec{u})^T - \frac{2}{3} \nabla \cdot \vec{u} \mathbf{I} \right] \quad (\text{A4})$$

where  $\mu$  is the apparent viscosity and  $\mathbf{I}$  is the identity tensor.

No-slip boundary conditions are assumed at the solid–fluid interface, where the casing may be static or may rotate at a constant angular velocity.

During cement placement/mud displacement, the mud may be left behind due to two-phase interface instability. In this work, we assume the cement displacement efficiency (CDE) is high enough that the volume of the non-displaced mud is small, and its impact on the cement front location is negligible. The volume of fluid (VOF) method is adopted to capture the two-phase interface. The annulus is initially filled with the displaced fluid, and from the beginning of the simulation, the displacing fluid is injected at the inlet. The volume factor of the cement as the displacing fluid is recorded during the simulation as the CDE. The simulation time is set such that three times the total volume flows through the annulus.

If the CDE is high enough, the impact of the non-displaced mud on the pressure is negligible. In this case, the model can be simplified to single-phase flow in each section. For the single-phase flow, a pre-load is applied to help the simulation converge to the steady-state flow faster. For the two-phase flow, the mesh of the annulus flow model is shown in Figure A1. The two-phase interface is shown in Figure A2.

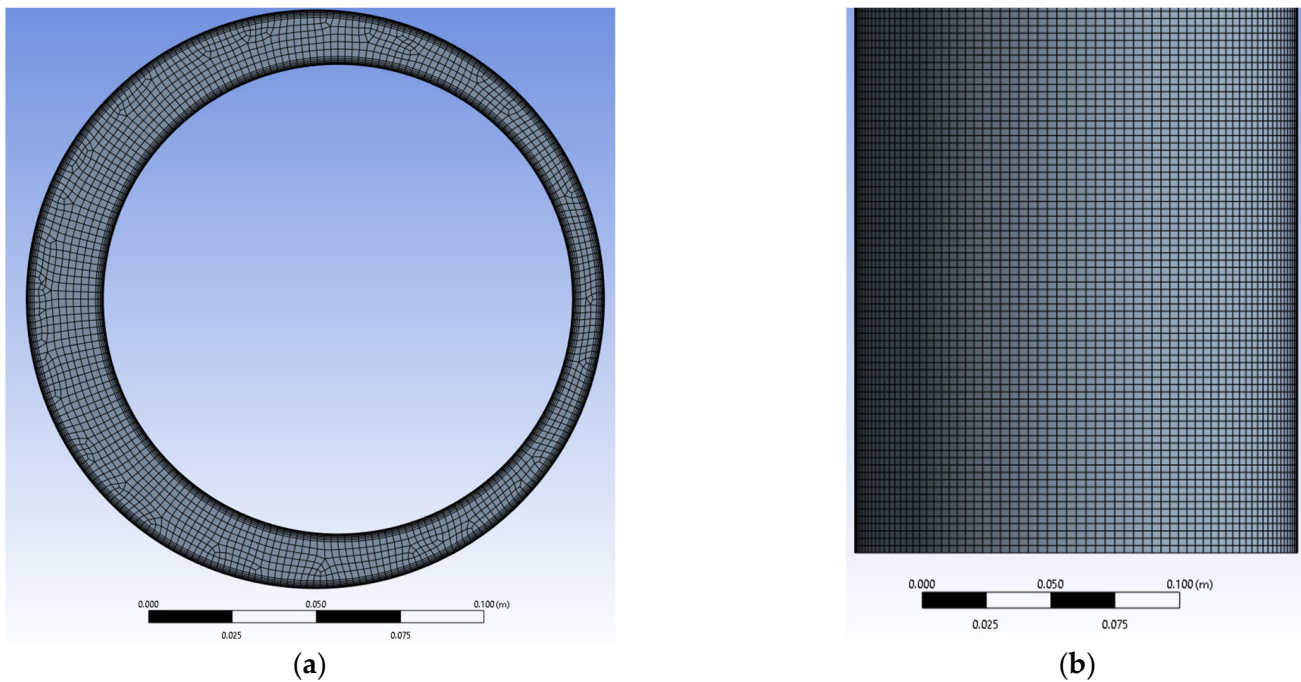


**Figure A1.** (a) Mesh of the annulus, top view. (b) Mesh of the annulus, side view.

The average pressures at the inlet and the outlet are monitored and recorded during the simulation. The pressure gradient is then calculated as the pressure difference between the inlet and outlet divided by the length of the model. Figure A3 shows the pressure gradient of the spacer flowing through the annulus using different numbers of elements in the mesh to demonstrate the convergence of the mesh.

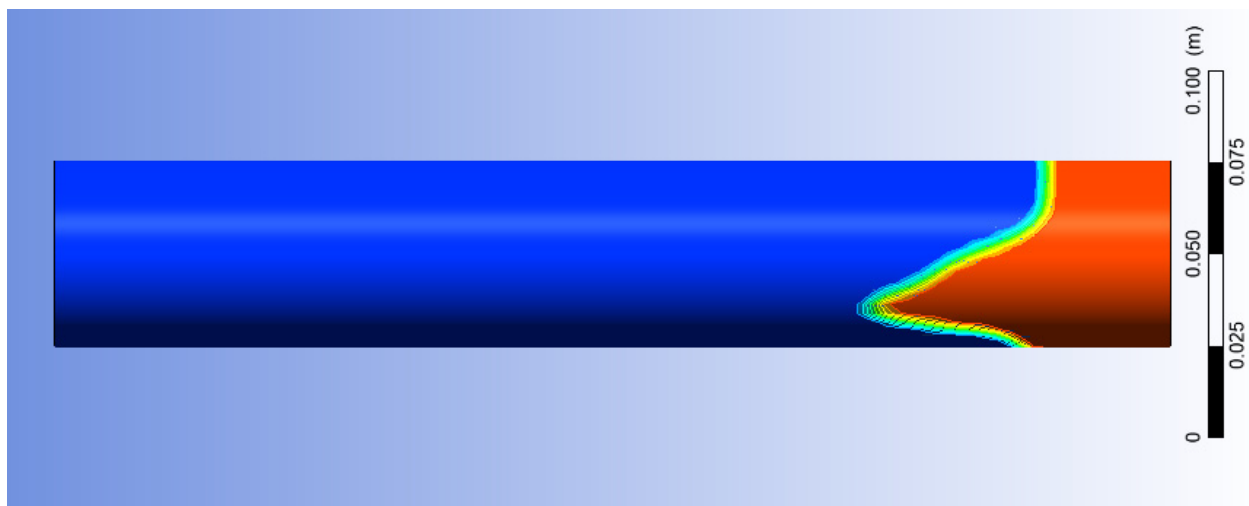


**Figure A2.** The two-phase interface during cement displacement. The flow direction is from left to right. The blue phase (cement) is the displacing fluid, and the red phase (spacer) is being displaced.

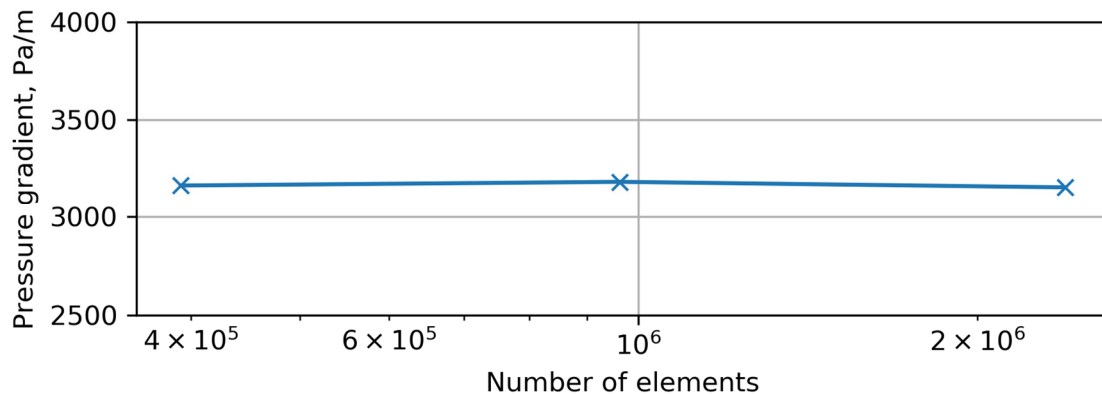


**Figure A3.** The steady-state pressure gradient of the spacer flow through the annulus using different numbers of elements.

## Appendix B. Wellbore Diameter Analysis and Data Fitting

To improve the accuracy of annular frictional pressure estimation, we look for more parameters to describe the wellbore geometry other than the average diameter for cement placement analysis. Figure A4 shows the histogram of the diameter distribution of a section in Well X acquired via ultrasonic well caliper log. As the wellbore diameter is impacted by many factors, it might follow a pattern along the measured depth and thus can be fitted with a distribution function.

With 844k+ data points, 89 distributions were fitted using maximum likelihood estimation (MLE). The 89 distributions are randomly put into six groups (to parallelize and accelerate the analysis), and the distributions with the lowest sum squared error (SSE) in each group are marked in the figure as well as the normal distribution (Gaussian distribution), as shown in Table A1. The Tukey lambda distribution has the lowest SSE of 21.1, but it is defined by the quantile function instead of the probability density function (PDF). Five other distributions were of similar SSE value (35–90). However, the normal distribution is at a much higher SSE value of 356. The mean absolute percentage error (MAPE) is also calculated and listed in Table A1. Without further evaluation of a larger dataset, which is beyond the scope of this paper, it is premature to conclude that any particular distribution is superior for the description of the wellbore diameter. However, the purpose of this appendix is to point out the fact that the wellbore diameter is not uniform but distributes

around an average diameter. The reader may also verify in Appendix C that a lower SSE or MAPE does not guarantee a better estimation of the average pressure gradient.

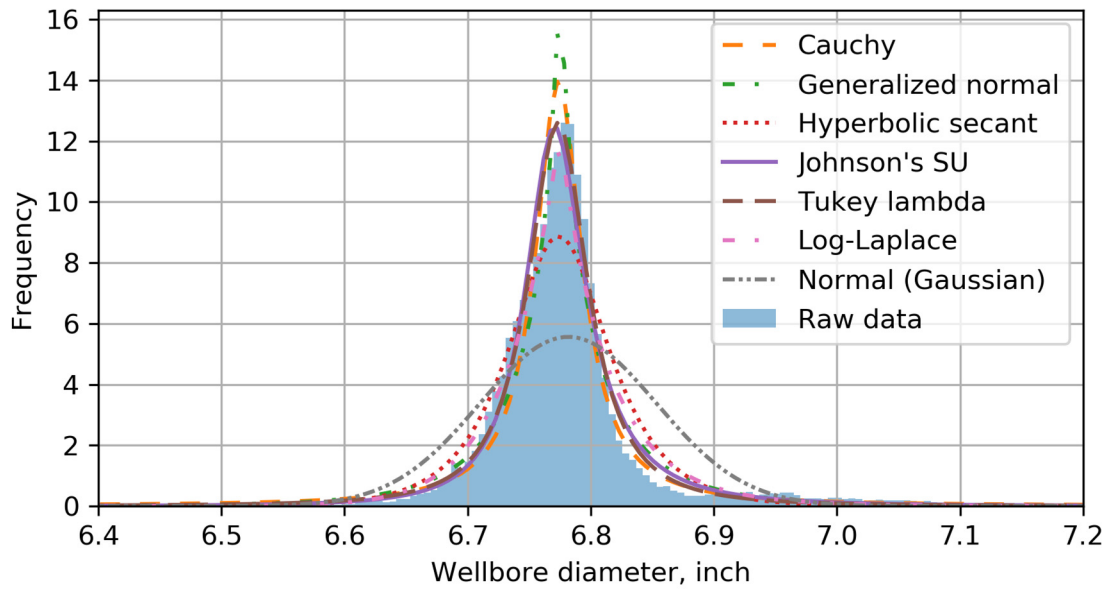


**Figure A4.** The wellbore diameter distribution in a lateral section in Well X. Seven fitted distributions are marked.

**Table A1.** Sum squared error (SSE) and mean absolute percentage error (MAPE) of seven continuous distributions.

Distribution Name	Number of Parameters ( $\sigma, \mu, \gamma, \lambda$ )	Probability Density Function $p(x)$	SSE	MAPE
Cauchy	2	$\frac{1}{\pi\sigma \left[1 + \left(\frac{x-\mu}{\sigma}\right)^2\right]}$	41.3	806
Generalized normal	3	$\frac{\gamma e^{-\left(\frac{x-\mu}{\sigma}\right)^\beta}}{2\sigma\Gamma\left(\frac{1}{\beta}\right)}$	57.6	136
Hyperbolic secant	2	$\frac{1}{2} \operatorname{sech}\left(\frac{\pi}{2} \frac{(x-\mu)}{\sigma}\right)$	89.3	80.8
Johnson's SU	4	$\frac{\lambda}{\sigma\sqrt{2\pi}} \frac{1}{\sqrt{1 + \left(\frac{x-\mu}{\sigma}\right)^2}} e^{-\frac{1}{2}[\gamma + \lambda \sinh^{-1}\left(\frac{x-\mu}{\sigma}\right)]^2}$	35.3	139
Tukey lambda	3	Tukey lambda is defined by the quantile function when location = 0 and scale = 1: $Q(p; \lambda) = \begin{cases} \frac{1}{\lambda} [p^\lambda - (1-p)^\lambda], & \text{if } \lambda \neq 0 \\ \log\left(\frac{p}{1-p}\right), & \text{if } \lambda = 0 \end{cases}$	21.1	276
Log-Laplace	2	$\frac{1}{2\sigma x} e^{-\frac{ \ln x - \mu }{\sigma}}$	43.9	75.0
Normal (Gaussian)	2	$\frac{1}{\sigma\sqrt{2\pi}} e^{-\frac{1}{2}\left(\frac{x-\mu}{\sigma}\right)^2}$	356	120

It might also be worth mentioning that the diameter distribution is slightly asymmetric (skewed), and the skewness of the wellbore diameter distribution is 1.97:

$$\frac{E[(d - \bar{d})^3]}{(E[(d - \bar{d})^2])^{\frac{3}{2}}} \approx \frac{\frac{1}{n} \sum_{i=1}^n (d_i - \bar{d})^3}{\left[\frac{1}{n} \sum_{i=1}^n (d_i - \bar{d})^2\right]^{\frac{3}{2}}} = 1.97 \tag{A5}$$

where  $\{d_i\}_{i=1}^n$  is the wellbore diameter dataset of  $n$  data points and  $\bar{d}$  is the average diameter. Thus, the skewness is potentially a factor to consider when looking for the optimal wellbore diameter distribution function.

### Appendix C. Annular Pressure Gradient Fitting and Interpolation

Most wells lack diameter measurement data, and it is especially difficult to estimate wellbore diameter in the design phase when running cementing software for planning purposes. To perform the analysis on these wells, we assume the wellbore diameter data follow some distribution which may be acquired from historical data of previous wells drilled in the same formation with similar well design and bottom hole assembly (BHA). In Appendix B, we have discussed the distribution of the wellbore diameter distribution in a measured well section. Assuming the probability density function  $p(d)$  of the wellbore diameter in a well section, the estimation of the pressure gradient in the annulus is:

$$E[\text{pressure gradient}] = E[f] = \int_0^{\infty} p(d)f(d)dd \quad (\text{A6})$$

where  $f(d)$  is the annular frictional pressure gradient as a function of the wellbore diameter  $d$  for a given set of fluid rheology and flow rate in the annulus outside a given casing.

Without an analytical solution of the annular flow, it is impossible to obtain the exact closed-form expression of the pressure gradient  $f(d)$ . In reality, the wellbore diameter is always finite and is usually larger than the casing diameter. Thus, we approximate the estimated pressure gradient by breaking the diameter distribution into  $N$  sections.

$$\begin{aligned} E[f] &\approx \sum_{i=1}^N f\left(d_{\min} + \left(i - \frac{1}{2}\right)\Delta d\right) \int_{d_{\min} + (i-1)\Delta d}^{d_{\min} + i\Delta d} p(d)dd \\ &= \sum_{i=1}^N f(\hat{d}_i) \int_{d_{\min} + (i-1)\Delta d}^{d_{\min} + i\Delta d} p(d)dd \end{aligned} \quad (\text{A7})$$

where  $\Delta d = (d_{\max} - d_{\min})/N$ ,  $d_{\max}$  and  $d_{\min}$  are the upper and lower limits of the wellbore diameter, respectively, and  $d_{\max} \geq \max(\{d_i\}_{i=1}^n) \geq \min(\{d_i\}_{i=1}^n) \geq d_{\min}$ , and  $\hat{d}_i = d_{\min} + \left(i - \frac{1}{2}\right)\Delta d$  is the average diameter in each diameter distribution section. The integral of the probability density function is usually represented by the cumulative distribution function (CDF).

From Equations (A6) and (A7), the required calculation cases of annular frictional pressure gradient reduce to a finite number. The pressure gradient needs to be simulated for each set of fluid rheology, flow rate, casing outer diameter, and casing centralizer. To further decrease the number of simulation cases, we approximate  $f(\hat{d}_i)$  in Equation (A7) by nonlinear interpolation.

For simplicity, we first fit a polynomial function of the wellbore diameter to the pressure gradient data using least square fitting and use the fitted function to estimate the pressure gradient at different wellbore diameters using a finite number of simulations. For post-job analysis, we use the fitted polynomial functions to estimate the pressure gradient at each diameter data point and obtain the average pressure gradient in the well section. Figure A5 shows the average pressure gradient calculated in this way using simulated pressure gradients at 5, 8, and 15 different wellbore diameters. The fitted (estimated) pressure gradient converges as the data points, and the order of polynomial equations increases. Figure A5 shows that the cubic polynomial fitted from 5 data points is of satisfactory precision and is only 0.1% smaller than the 6th-order polynomial fitted from 15 data points. To avoid potentially misleading results from overfitting, the number of parameters in the fitting function must be significantly lower than the raw data points.

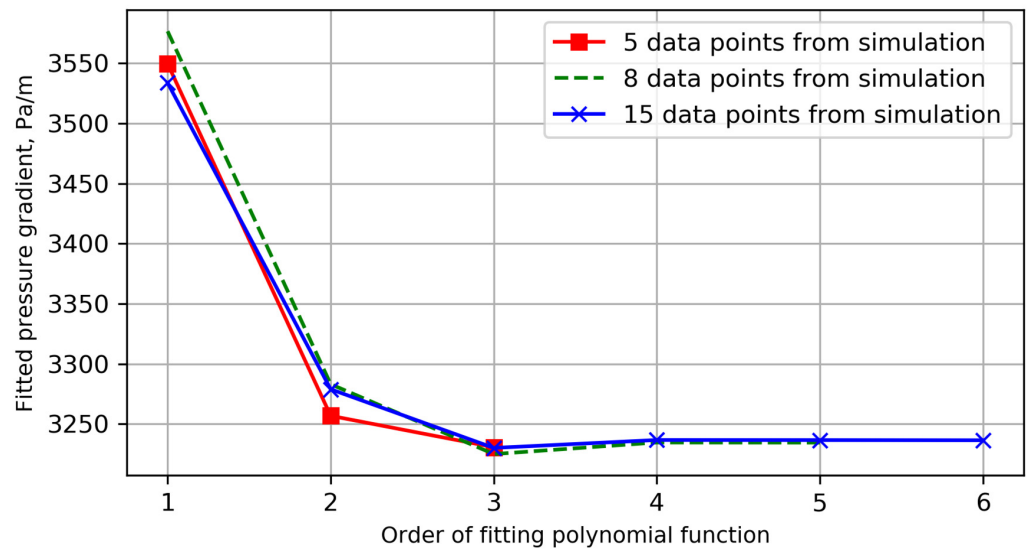


**Figure A5.** The average pressure gradient of the spacer at a pump rate of 4.4 bpm in the well section is described in Figure A4. Polynomial functions of different orders are fitted to different numbers of data points from the simulation. The pressure gradient at each measured wellbore diameter is then calculated using the polynomial functions.

If we further select the  $d_{min}$  and the  $d_{max}$  values such that  $P(d \leq d_{min}) = 0.0001$  and  $P(d \leq d_{max}) = 0.9999$ , we can calculate the estimated pressure using Equation (A7). For convenience, we call  $\hat{d}_i$  the interpolation points because the pressure gradient at these wellbore diameters is interpolated using the polynomial functions. The impact of the number of interpolation points is shown in Figure A6 for the six distributions using 10, 20, 50, 100, 200, 500, and 1000 interpolation points and a 5th-order polynomial function. The results start to converge at about 50 interpolation points. The estimated pressure gradient using the raw diameter data from Figure A5 is plotted in a dashed black line and used as the benchmark pressure gradient. The results from the Cauchy distribution are found to diverge as the interpolation points increase and are not plotted. The MAPE of the Cauchy distribution is the highest. The Tukey lambda distribution has the second-highest MAPE and also performed poorly. However, lower MAPE does not guarantee better performance among the other distributions.

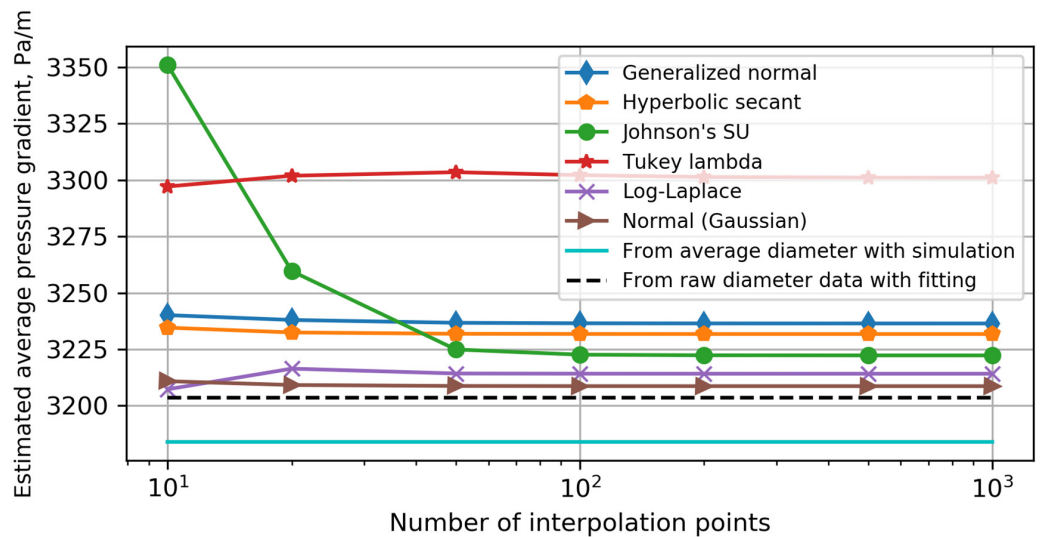


**Figure A6.** Estimated pressure gradient converges as the number of interpolation points increases for the 6 distributions.

Figure A7 shows the estimated pressure gradient by different assumed distributions using 15 data points from simulation and 1000 interpolation points. The estimated pressure gradient using the raw diameter data from Figure A5 is plotted in a dashed black line and used as the benchmark pressure gradient. The results from most distributions converge at the 3rd polynomial function, while the result from the Cauchy distribution diverges and is not plotted. Surprisingly, the normal distribution provides the best accuracy with a relative error of <0.16%; however, it also had the largest SSE among all six distributions in Figure A7. Similarly, MAPE alone does not reflect the relative performance of the different distribution functions. The pressure gradient simulated using the average wellbore diameter has a 0.62% relative error.

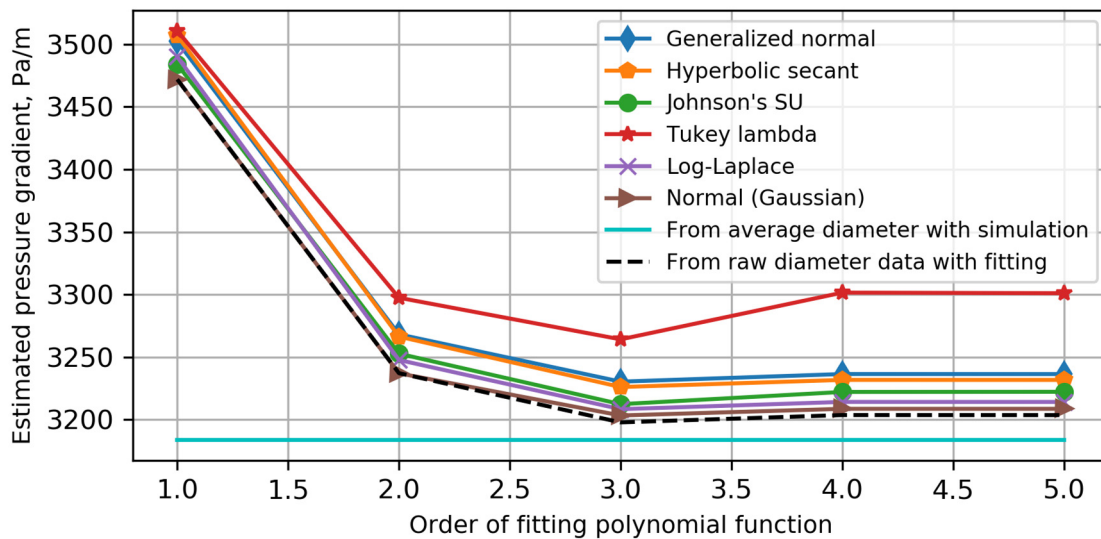


**Figure A7.** The estimated pressure gradient converges as the order of the fitting polynomial function increases for the 6 distributions.

To achieve the best pressure gradient estimation accuracy, the optimal distribution function can only be selected following the analysis shown in Figure A7, and a simple criterion such as using the SSE or MAPE has not yet been found. Therefore, it is left outside of the scope of this paper.

Even though the improvement in estimation accuracy of adopting a certain wellbore distribution is marginal, it might still be recommended. In large-scale applications, the pressure gradient at different combinations of the rheology, wellbore geometry, and flow rate can be experimentally measured or numerically simulated (as in this paper) and then stored in a database. Thus, the pressure analysis of each individual well does not require an excessive number of measurements or simulations. However, for one-time analysis without prior knowledge of the pressure gradient, the pressure analysis can be based on the average wellbore diameter with reasonable accuracy.

A similar interpolation strategy can be applied to other impact parameters, including the flow rate, rheological parameters, and casing outer diameter. However, simple interpolation functions of the type  $f(x_1, \dots, x_n) = \prod_{i=1}^n g_i(x_i)$  performed poorly and the results are not shown here. It is possible to sequentially interpolate along the flow rate and then interpolate along the wellbore diameter with careful testing because the relation between the pressure gradient and the flow rate is almost linear. The strategy and/or proper interpolation function is open to future research.

The impact of temperature can be introduced by a one-way coupling strategy. Firstly, the temperature profile in the well is estimated using the method described by Khaled et al. [30]. Secondly, the equivalent average viscosity of each fluid in each well section is determined using the same interpolation strategy described in this appendix. Finally, the equivalent average viscosity is used as the viscosity in the modeling method.

## References

1. Nelson, E.B.; Guillot, D. (Eds.) *Well Cementing*, 2nd ed.; Schlumberger: Sugarland, TX, USA, 2006.
2. Enayatpour, S.; van Oort, E. Advanced modeling of cement displacement complexities. In Proceedings of the SPE/IADC Drilling Conference and Exhibition, The Hague, The Netherlands, 14–16 March 2017. [\[CrossRef\]](#)
3. Foroushan, H.K.; Bjørnar, L.; Jan, D.Y.; Arild, S. Cement Placement: An Overview of Fluid Displacement Techniques and Modelling. *Energies* **2021**, *14*, 573. [\[CrossRef\]](#)
4. Zheng, D.; Miska, Z.; Ozbayoglu, E.; Zhang, Y. The Influence of Elliptical-Geometry Wellbore on Zonal Isolation. In Proceedings of the 56th U.S. Rock Mechanics/Geomechanics Symposium, Santa Fe, NM, USA, 26–29 June 2022. [\[CrossRef\]](#)
5. McLean, R.H.; Manry, C.W.; Whitaker, W.W. Displacement mechanics in primary cementing. *J. Pet. Technol.* **1967**, *19*, 251–260. [\[CrossRef\]](#)
6. Beirute, R.M.; Flumerfelt, R.W. Mechanics of the displacement process of drilling muds by cement slurries using an accurate rheological model. In Proceedings of the SPE Annual Fall Technical Conference and Exhibition, Denver, CO, USA, 9–12 October 1977. [\[CrossRef\]](#)
7. Sun, J.; Li, Z.; Luo, P.; Huang, S. Numerical modeling of motion of displacement interface in eccentric annulus during primary cementing. *Energy Sci. Eng.* **2020**, *8*, 1579–1591. [\[CrossRef\]](#)
8. Wu, Z.; Chen, Z.; Zhao, Y.; Xue, Y.; Wang, C.; Xiong, C.; Chen, S. Theoretical and Experimental Study on Cementing Displacement Interface for Highly Deviated Wells. *Energies* **2023**, *16*, 733. [\[CrossRef\]](#)
9. Savery, M.; Darbe, R.; Chin, W. Modeling fluid interfaces during cementing using a 3D mud displacement simulator. In Proceedings of the Offshore Technology Conference, Houston, TX, USA, 30 April–3 May 2007. [\[CrossRef\]](#)
10. Pks, S.; Yerubandi, K.B. Slim-Well Completions: A 3D Numerical Approach for Displacement to Design Effective Cementing Fluids. In Proceedings of the Trinidad and Tobago Energy Resources Conference, Port of Spain, Trinidad, 27–30 June 2010. [\[CrossRef\]](#)
11. Chiney, A.; Yerubandi, K.B. 3D Displacement Simulator Realistically Predicts Free Fall during Cementing. In Proceedings of the SPE/IADC Middle East Drilling Technology Conference & Exhibition, Dubai, United Arab Emirates, 7–9 October 2013. [\[CrossRef\]](#)
12. Chen, Z.; Chaudhary, S.; Shine, J. Intermixing of cementing fluids: Understanding mud displacement and cement placement. In Proceedings of the IADC/SPE Drilling Conference and Exhibition, Fort Worth, TX, USA, 4–6 March 2014. [\[CrossRef\]](#)
13. Gao, H.; Ai, Z.; Zhang, J.; Zhou, B.; Chen, F.; Wang, W.; Liu, Z.; Deng, Q.; Shi, Y.; Wang, Z. Numerical Simulation of Improving Cementing Displacement Efficiency under Narrow Safety Density Window. In Proceedings of the SPE/IATMI Asia Pacific Oil & Gas Conference and Exhibition, Bali, Indonesia, 29–31 October 2019. [\[CrossRef\]](#)
14. Bu, Y.; Tian, L.; Li, Z.; Zhang, R.; Wang, C.; Yang, X. Effect of casing rotation on displacement efficiency of cement slurry in highly deviated wells. *J. Nat. Gas Sci. Eng.* **2018**, *52*, 317–324. [\[CrossRef\]](#)
15. Tardy, P.M.J.; Bittleston, S.H. A model for annular displacements of wellbore completion fluids involving casing movement. *J. Pet. Sci. Eng.* **2015**, *126*, 105–123. [\[CrossRef\]](#)
16. Tardy, P.M.; Flamant, N.C.; Lac, E.; Parry, A.; Utama, C.S.; Almagro, S.P. New generation 3D simulator predicts realistic mud displacement in highly deviated and horizontal wells. In Proceedings of the SPE/IADC Drilling Conference and Exhibition (p. D021S011R004), The Hague, The Netherlands, 14–16 March 2017; SPE: Kuala Lumpur, Malaysia, 2017. [\[CrossRef\]](#)
17. Bogaerts, M.; Cardozo, J.; Flamant, N.; Giam, D.; Villar, V.; Lehr, J. Novel 3D Fluid Displacement Simulations Improve Cement Job Design and Planning in the Gulf of Mexico. In Proceedings of the SPE Annual Technical Conference and Exhibition, Calgary, AB, Canada, 30 September–2 October 2019. [\[CrossRef\]](#)
18. Tardy, P.M. A 3D model for annular displacements of wellbore completion fluids with casing movement. *J. Pet. Sci. Eng.* **2018**, *162*, 114–136. [\[CrossRef\]](#)
19. Foroushan, H.K.; Ozbayoglu, E.M.; Gomes, P.J.; Yu, M. Mud/cement displacement in vertical eccentric annuli. *SPE Drill. Complet.* **2020**, *35*, 297–316. [\[CrossRef\]](#)
20. Maleki, A.; Frigaard, I. Primary cementing of oil and gas wells in turbulent and mixed regimes. *J. Eng. Math.* **2017**, *107*, 201–230. [\[CrossRef\]](#)
21. Jung, H.; Frigaard, I.A. Evaluation of common cementing practices affecting primary cementing quality. *J. Pet. Sci. Eng.* **2022**, *208*, 109622. [\[CrossRef\]](#)
22. Zhang, Z.; Huang, Z.; Zhou, Y.; Sheng, M.; Wu, B. Characteristic of Spiral Displacement Process in Primary Cementing of Vertical Well Washout. *SPE J.* **2023**, *28*, 509–521. [\[CrossRef\]](#)
23. Li, X.; Novotny, R.J. Study on cement displacement by lattice-Boltzmann method. In Proceedings of the SPE Annual Technical Conference and Exhibition, San Antonio, TX, USA, 24–27 September 2006. [\[CrossRef\]](#)
24. Grasinger, M.; Li, Z.; Vuotto, A.; Brigham, J.; Iannacchione, A.; Vandenbossche, J. Simulation of cement slurry flow to assess the potential for voids and channels in wellbore cementing processes. In Proceedings of the SPE Eastern Regional Meeting, Morgantown, WV, USA, 13–15 October 2015. [\[CrossRef\]](#)
25. Dixon, J.C. *The Shock Absorber Handbook*; John Wiley & Sons: Chichester, UK, 2008.
26. Chilton, R.A.; Stainsby, R. Pressure loss equations for laminar and turbulent non-Newtonian pipe flow. *J. Hydraul. Eng.* **1998**, *124*, 522–529. [\[CrossRef\]](#)
27. Wang, N.; Cheng, Z.; Lu, Y.; Jiang, W.; Zhou, J.; He, B.; Ren, G. A multibody dynamics model of contact between the drillstring and the wellbore and the rock penetration process. *Adv. Mech. Eng.* **2015**, *7*, 35–51. [\[CrossRef\]](#)

28. Amani, M.; Al-Jubouri, M.; Shadravan, A. Comparative study of using oil-based mud versus water-based mud in HPHT fields. *Adv. Pet. Explor. Dev.* **2012**, *4*, 18–27. [[CrossRef](#)]
29. Vajargah, A.K.; van Oort, E. Determination of drilling fluid rheology under downhole conditions by using real-time distributed pressure data. *J. Nat. Gas Sci. Eng.* **2015**, *24*, 400–411. [[CrossRef](#)]
30. Khaled, M.S.; Wang, N.; Ashok, P.; van Oort, E. Downhole heat management for drilling shallow and ultra-deep high enthalpy geothermal wells. *Geothermics* **2023**, *107*, 102604. [[CrossRef](#)]
31. Khaled, M.S.; Wang, N.; Ashok, P.; Chen, D.; van Oort, E. Strategies for Prevention of Downhole Tool Failure Caused by High Bottomhole Temperature in Geothermal and High-Pressure/High-Temperature Oil and Gas Wells. *SPE Drill. Complet.* **2023**, *38*, 243–260. [[CrossRef](#)]
32. Fakoya, M.F.; Ahmed, R.M. A generalized model for apparent viscosity of oil-based muds. *J. Pet. Sci. Eng.* **2018**, *165*, 777–785. [[CrossRef](#)]

**Disclaimer/Publisher’s Note:** The statements, opinions and data contained in all publications are solely those of the individual author(s) and contributor(s) and not of MDPI and/or the editor(s). MDPI and/or the editor(s) disclaim responsibility for any injury to people or property resulting from any ideas, methods, instructions or products referred to in the content.